ISMRM ANZ 4th Annual Chapter Meeting

Peer-Reviewed Abstracts

Table of Contents

Oral Session 1: Revolutionising MRI technology

Study design for mobile Point of Care MR (PoCeMR) network in Australia – **Zhaolin Chen**

Zhaolin Chen[1], Shenjun Zhong[1], Parisa Zakavi[1], Kh Tohidul Islam[1], Gail Durbridge[2], Helen Kavnoudias[3,9], Christen Barras[4], Shawna Farquharson[5], Andrew Dwyer[6], Paul M. Parizel[7,8], Meng Law[3,9], Markus Barth[10], Katie McMahon[11], and Gary Egan[1]

[1] Monash Biomedical Imaging, Monash University, Victoria; [2] Herston Research Imaging Facility, University of Queensland; [3] Alfred Hospital, Victoria; [4] Royal Adelaide Hospital, South Australia; [5]Australian National Imaging Facility; [6] South Australian Health and Medical Research Institute, South Australia; [7] Royal Perth Hospital (RPH), Western Australia; [8] Medical School, University of Western Australia (UWA); [9] iBRAIN Monash University; [10] Centre for Advanced Imaging, University of Queensland. [11] School of Clinical Science, Herston Imaging Research Facility, Queensland University of Technology.

Introduction

Mobile point-of-care medical devices, such as point-of-care low-field MRI (PoCeMR), have the potential to revolutionise how people receive medical treatment[1]. Mobile devices can provide timely and adequate care to people in need and open the opportunity to address healthcare inequality in rural and remote locations[2]. Recent studies in brain injury patients suggest that PoCeMR can be successfully deployed in intensive care units[3,4]. This study aims to establish a nationwide capability of point-of-care MR imaging using artificial intelligence inspired improved image quality to assess the clinical utility for stroke and traumatic brain injury.

Methods

Healthy subjects as well as stroke and brain injury patients will undergo MR scanning using the 65mT ultra-low-field Swoop (Hyperfine Inc. USA) and routine superconductive scanners (1.5T and 3T) at five sites in Australia (Monash University, University of Queensland, The Alfred Hospital, Royal Adelaide Hospital, and Royal Perth Hospital). Human Research Ethics have been approved for both healthy subjects and patients to participate in this research. The data acquisition and storage protocol include collection of image pairs (T1-weighted, T2-weighted, FLAIR and DWI), and storage of raw (k-space) datasets. To share and aggregate data from multiple sites, all data will be de-identified and sent to a centralized XNAT over a secure channel to comply with the ethics and data privacy policies.

Results

Initial scans from the Swoop scanner demonstrate the feasibility to acquire T1, T2, FLAIR, and DWI images. Careful positioning of the subject is required for optimal image quality and workflow efficiency.

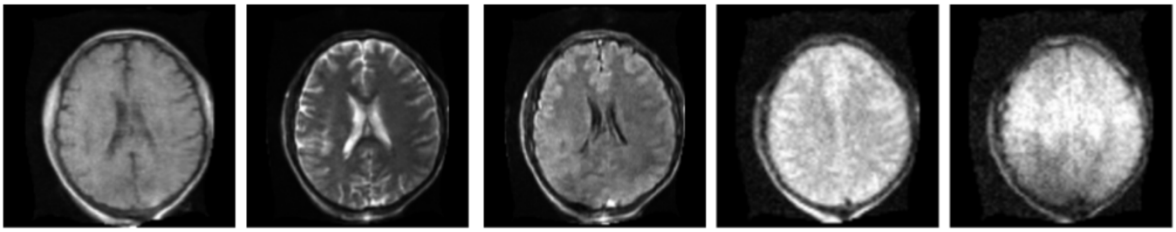

Figure 1: Preliminary scans from the Swoop Hyperfine mobile MR scanners in the national PoCeMR network.

Discussion and Conclusion

The aim of the PoCeMR network is to directly address a National Gap in the current Australian imaging capability to support the diagnostic imaging requirements for rural and remote Australians. The network architecture will facilitate knowledge sharing, develop a raw data repository for the research community, and facilitate the translation of point of care mobile MR scanners into routine clinical practice. The ability of artificial intelligence models to enhance image quality and clinical usability will be investigated.

References

[1]Karlen, W. (Ed.). (2015). Mobile Point-of-Care Monitors and Diagnostic Device Design (1st ed.). CRC Press. [2]Commonwealth of Australia (2018) Availability and Accessibility of Diagnostic Imaging Equipment around Australia, Department of the Senate. [3]Sheth KN, Mazurek MH, Yuen MM, et al. (2021) Assessment of Brain Injury Using Portable, Low-Field Magnetic Resonance Imaging at the Bedside of Critically Ill Patients. JAMA Neurol. 78(1):41-47. [4] Mazurek, M.H., Cahn, B.A., Yuen, M.M. et al. (2021) Portable, bedside, low-field magnetic resonance imaging for evaluation of intracerebral hemorrhage. Nat Commun 12, 5119.

Advancing Ultralow Field MRI with Deep Learning Reconstruction – **David Waddington**

David E. J. Waddington[1], Efrat Shimron[2], Shanshan Shan[1], Neha Koonjoo[3] Matthew S. Rosen[3]

[1]Image X Institute, Faculty of Medicine and Health, The University of Sydney, Australia

[2]Department of Electrical Engineering and Computer Sciences, UC Berkeley, CA, USA

[3]A. A. Martinos Center for Biomedical Imaging, Massachusetts General Hospital, MA, USA

Introduction

Portable MRI scanners that operate at very low magnetic fields are increasingly being deployed in clinical settings. However, the intrinsic low signal-to-noise ratio (SNR) of these low-field MRI scanners often necessitates many signal averages, and therefore, excessively long acquisition times. Advanced reconstruction strategies based on deep learning could dramatically shorten acquisition times in low-field MRI when combined with undersampling. Here, we compare leading data-driven[1] and model-driven[2] deep learning frameworks to gold-standard compressed sensing (CS) for the reconstruction of ultralow field MRI data.

Methods

Phantom experiments were performed on a 6.5 mT MRI scanner with a quadrature head coil and a brain-shaped phantom.[3] A 3D Cartesian balanced-steady state free precession (bSSFP) sequence with TR/TE = 22/11 ms and matrix size 64 x 75 x 25 (Readout x Phase Encode 1 x Phase Encode 2) was used for acquisition with 256 signal averages. K-space was retrospectively 4× undersampled in the phase-encode dimensions with a Poisson-disc (PD) mask. Human data were prospectively acquired with a 2× undersampled PD mask and 40 signal averages (~7 min. acquisition).

Data-driven AUTOMAP[1] and model-driven Unrolled Optimization[2] reconstruction networks were implemented as described in Refs 4 and 5, respectively. A training corpus of 50,000 brain image/k-space pairs were used for network training with k-space data undersampled with PD masks at the desired reduction factors (R=2 or 4). To reconstruct 3D data, a 1D FFT was applied along the fully-sampled readout dimension and trained networks were applied to the undersampled hybrid k-space.

For CS reconstruction, sensitivity maps were calculated with ESPIRiT, and L1-wavelet CS reconstruction was performed using SigPy.[4] Normalized root-mean-square error (NRMSE) and structural similarity (SSIM) reconstruction metrics were calculated relative to the fully-sampled ground-truth acquisition.

Results

Reconstructions of 4× undersampled phantom data are shown in Figure 1a. Reconstruction with AUTOMAP yielded the highest/best structural similarity metric, while CS reconstruction gave the lowest/best NRMSE metric. CS and unrolling network images demonstrate sharper reconstructed edges. Human brain images prospectively acquired with PD undersampling (R=2) and reconstructed via AUTOMAP are shown in Figure 1b.

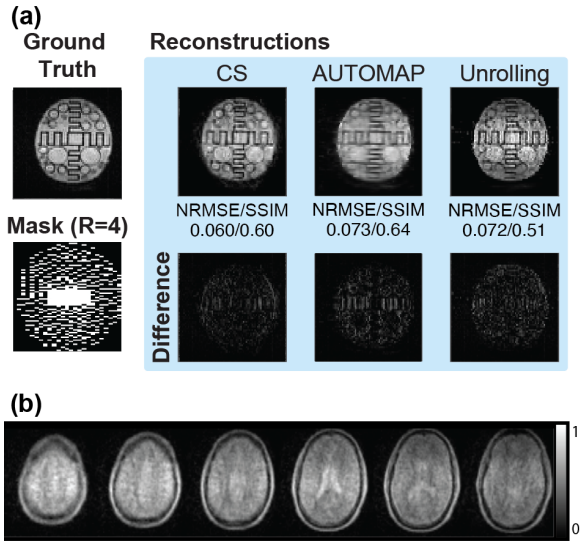

Figure 1: (a) Comparison of image reconstruction accuracy for Compressed Sensing (CS), AUTOMAP, and Unrolling Network techniques with R=4. (b) AUTOMAP-based reconstruction of an R=2, sub-7-minute scan of the human brain at 6.5 mT. The central 6 slices are shown.

Discussion and Conclusion

Undersampling is an effective means to shorten long MR acquisitions. Our findings demonstrate that AUTOMAP can improve structural similarity, as compared to CS, when reconstructing undersampled data. Prospective deployment of PD undersampling will enable the clinical utility of deep learning reconstruction to be tested on low field MRI scanners. These results will inform the development of faster imaging strategies for portable MRI.

References

1. Zhu et al., *Nature*, **555**, 487-492 (2018).
2. Zhang et al. *IEEE CVPR*, 1828-1837 (2018).
3. Sarracanie M et al., *Sci Rep*., **5,** 15177 (2015).
4. Koonjoo et al., *Sci Rep.,* 8248 (2021).
5. Shan et al., *arXiv*, 2205.10993 (2022).
6. Ong F et al., ISMRM Ann. Meeting, 4819 (2019).

Improving the robustness of deep learning segmentation models by analysing intensity distribution shifts between data sets – **Fernanda Ribiero**

Fernanda L Ribeiro[1], Xincheng Ye[1], Trevor A Mori[2], Lawrence J Beilin[2], Markus Barth[1], and Steffen Bollmann[1]

[1]School of Information Technology and Electrical Engineering, The University of Queensland; Brisbane; Australia
[2]Medical School, The University of Western Australia; Perth; Australia

Introduction

Deep learning could revolutionize medical imaging applications. However, progress is currently held back by the lack of model generalizability and reliability. One such drawback is, for example, the very fact that deep learning models' accuracy often deteriorates when they are deployed in a new/unseen dataset. Indeed, we recently deployed a pre-trained deep learning model [1] for abdominal adipose tissue (AAT) segmentation in appropriately pre-processed abdominal images and found that the model did not perform as expected (Figure 1a). The original dataset on which the model was trained is not openly available; hence, it is not possible to match our data to the training data. Here we propose an analysis of intensity distributions to determine the optimal range of intensity values for each class prediction of an existing deep learning model without fine-tuning or retraining.

Methods

We used an abdominal Dixon MRI dataset to determine how intensity value distributions affect the performance of FatSegNet, the pre-trained deep learning model for visceral and subcutaneous fat segmentation. This dataset includes abdominal images from 975 Gen2 participants at 27-years of age from the Raine Study in Perth, WA, using a Siemens Magnetom Espree 1.5T (Siemens AG, Erlangen, Germany). FatSegNet was originally trained using the Rhineland Study dataset [1], which includes abdominal MR Dixon scans. Specifically, the model was trained on 38 manually annotated datasets. For AAT segmentation, 60 slices per participant were manually labelled into three classes: subcutaneous adipose tissue (SAT), visceral adipose tissue (VAT), and bone with neighbouring tissues.

Results and Discussion

Figure 1a shows the original data from one participant with the segmentation generated by FatSegNet. As can be seen, the model fails to appropriately segment SAT and VAT, which can be better appreciated by inspecting the overlapping distributions of intensity values across the three classes (Figure 1b). Following that, we found that by scaling the original image, it was possible to improve the segmentation results (Figure 1c). This finding is likely because the new distributions of intensity values peak in different intensity range for SAT and VAT labels (Figure 1d). Our preliminary result suggests that it may be possible to find the optimal range of input values for each class of a segmentation task, which could extend the usability and generalizability of deep learning models in medical imaging applications.

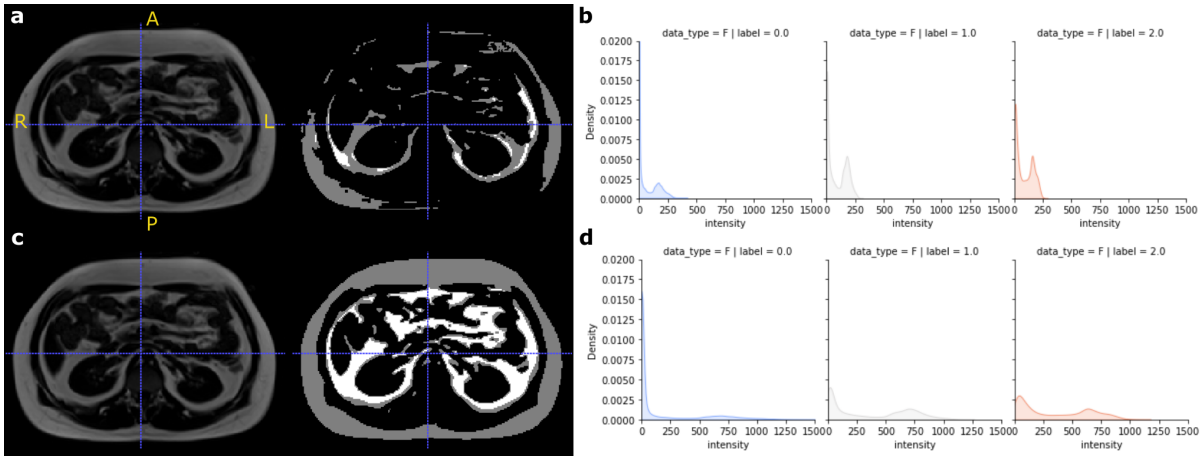

Figure 1 - ATT segmentation results. Label 0/black: bone with neighbouring tissues, Label 1/grey: SAT, and Label 2/white: VAT.

References

[1] S. Estrada *et al.*, "FatSegNet: A fully automated deep learning pipeline for adipose tissue segmentation on abdominal dixon MRI," *Magn Reson Med*, 2020.

Acknowledgements

This work was supported by the Australian Research Council (LP200301393). The MRI data were acquired by Envision Medical Imaging, Perth WA. The Raine Study was funded by the NH&MRC (Mori, APP 1102106).

Automatically Resampling Oblique-Acquired MRI to Enable Robust and Accurate QSM Algorithms – **Ashley Stewart**

***Ashley Stewart*[1], *Korbinian Eckstein*[1], *Thanh Thuy Dao*[1], *Kieran O'Brien*[2], *Josef Pfeuffer*[2], *Jin Jin*[2], *Markus Barth*[1], *Steffen Bollmann*[1]**

[1]School of Information Technology and Electrical Engineering, The University of Queensland, Brisbane, Australia;
[2]Siemens Healthineers Pty Ltd., Brisbane, Australia

Introduction: In an MRI acquisition, oblique slice orientations are often used to visualise clinically relevant anatomical regions and optimise the scanning field of view and duration. In Quantitative Susceptibility Mapping (QSM), which aims to estimate the magnetic susceptibility of tissues, many emerging algorithms assume that the main magnetic field is oriented axially through the imaging volume, which is not the case for oblique acquisitions. This assumption prevents accurate susceptibility quantification and introduces pervasive artefacts in susceptibility maps, limiting the practical uptake of the method. Recent work has identified resampling slices to an axial orientation prior to QSM processing as a solution[1]. In this work, we implement this rotate-and-resample method to enable automated processing of oblique acquisitions and publish it as part of the QSMxT software toolbox[2,3]. We test the implementation in silico using the QSM challenge head phantom, measuring differences in the effect of orientation on susceptibility quantification across brain regions, identifying that small sources such as veins remain challenging to quantify accurately after resampling. **Methods: Data:** The QSM challenge 2.0 *in silico* head phantom[4] was used for this experiment and is based on a segmented MP2RAGE dataset with 0.64 mm^3 isotropic resolution down-sampled to 1 mm^3 using k-space cropping and TEs=4/12/20/28 ms. The magnitude and phase were augmented by rotation about the x-axis to produce new datasets with effective B_0 directions at 5° increments up to 45°. **Processing:** Magnitude and phase data were resampled to an axial affine through the complex domain using nilearn prior to QSM processing using TGV-QSM[5]. The susceptibility maps were then resampled back to the original orientation. In QSMxT, this process occurs automatically when the obliquity, measured using nibabel, is greater than a user-defined threshold. **Measurements:** RMSE was measured across brain regions defined by segmentations provided with the original head phantom.

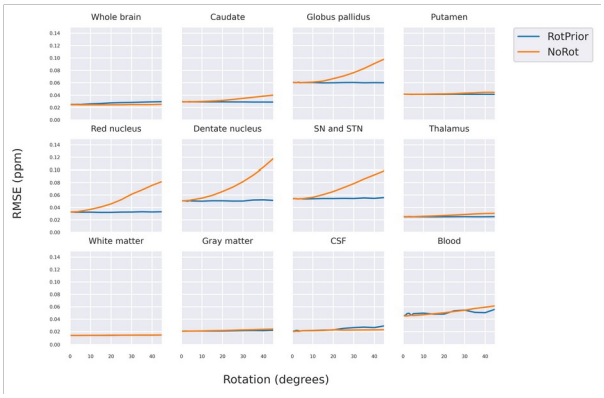

Results: RMSE measured in the head phantom indicates that the rotate-and-resample method (RotPrior) provides stable RMSEs across brain regions except in blood and CSF (see Figure 1). Conversely, no corrections (NoRot) cause increasing RMSE with the degree of rotation, particularly in deep gray matter (dGM) nuclei.**Figure 1**: RMSE with rotation, with and without rotate-and-resample using TGV-QSM.

Difference imaging visualises the spatial distribution of changes in susceptibility quantification and smearing artefacts in dGM regions as the degree of rotation increases (see Figure 2).

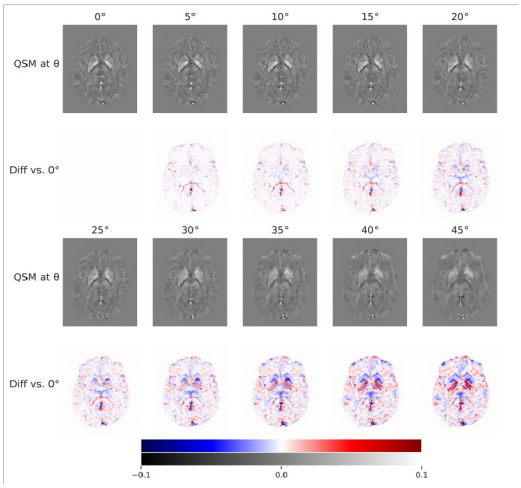

Figure 2: QSM computed using TGV-QSM on simulated data under various degrees of rotation, including difference images computed with respect to the zerodegrees rotated result.

Discussion and Conclusions: Our experiment validates that the rotate-and-resample method[1] results in stable susceptibility quantification across most brain regions. Further, small, high-susceptibility sources such as blood in veins were found to be more challenging to recover after resampling, which may be explained by reduced phase accuracy after interpolation in the complex domain. Our publicly available implementation of the method in QSMxT makes it available and practical for users wishing to reconstruct QSM for acquisitions with oblique slice orientations. **References:** 1] Kiersnowski et al. ISMRM 2021, Abstract 794. 2] Stewart et al., Mag. Reson. Med., 2022. 3] Stewart et al., QSMxT, GitHub, 2022.
4] Marques et al., Mag. Reson. Med., 2021. 6] Langkammer et al., NeuroImage, 2015.

Sub-Population Universal Pulses: A Feasibility Study – **Igor Tyshchenko**

***Igor Tyshchenko*[1], *Jin Jin*[2], *Simon Lévy*[2], *Bahman Tahayori*[3], *Leigh Johnston*[1]**

[1]Biomedical Engineering & Melbourne Brain Centre Imaging Unit, The University of Melbourne, Australia, [2]Siemens Healthcare Pty Ltd, Australia, [3]The Florey Institute of Neuroscience and Mental Health, Australia

Introduction

Universal parallel transmission (pTx) pulses are limited in performance because they encompass a large population distribution. We hypothesised that designing universal pulses (UP) based on sub-populations with reduced anatomic variability would improve the homogeneity and SAR performance in head imaging.

Methods

A generic 8-ch pTx coil model was tuned and matched for the Duke V3.0 (IT'IS, Zurich, Switzerland) anatomy. The three most SAR-sensitive head model parameters were selected: head breadth (HB), head length (HL) and Y-shift [1]. All parameters were modelled as Gaussian random variables with means μ_i and standard deviations σ_i of a Caucasian population [2]. Several sub-populations were studied by reducing the σ_{HB}, σ_{HL} and σ_Y to 50% and 25% of their original values. 21 representative anatomies were generated for each population following the multivariate and univariate unscented transform sampling scheme [3]. For each sub-population, a 5kT-UP inversion pulse was computed using the active-set MATLAB algorithm (The Mathworks, Natick, MA) [4, 5], based on the B_1^+-maps and Q-matrices derived from FDTD simulation (Sim4Life by ZMT, Zürich, Switzerland). An additional six test anatomies unseen by the pulse design algorithm were selected at $\pm\sigma_i$ for each parameter. The SAR distribution was studied by fitting a second-order polynomial and generating 10^6 samples [1].

Results & Discussion

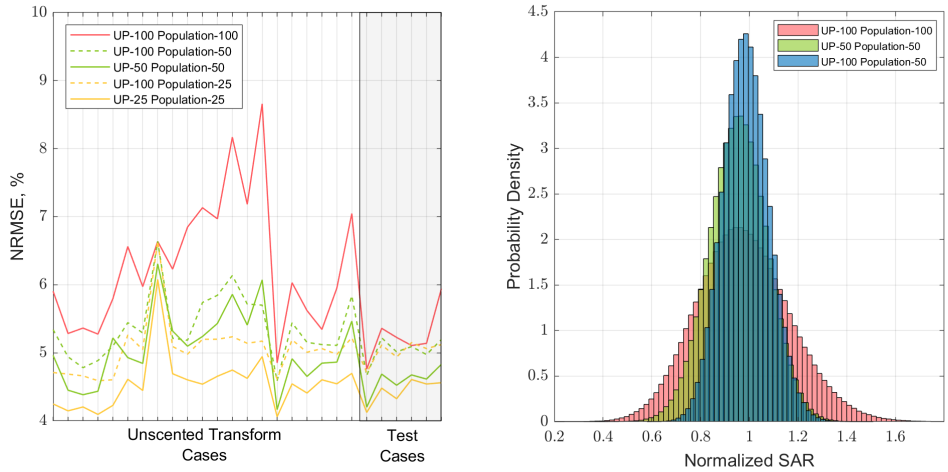

Figure 2. Left: pulse performance as measured by the normalised root mean square error (NRMSE) on the target flip angle. Right: SAR distribution normalised to the baseline value. UP-100 Population-50 represents UP designed based on 100% sub-population evaluated using 50% sub-population.

Reducing the population size results in an NRMSE improvement (Fig.1 left). The smaller volume of interest describing representative anatomies explains this reduction. By contrast, halving the population distribution reduces the SAR variability by around 40% (Fig.1 right). This means a less restrictive safety margin can be used, making the pulse design more SAR efficient.

Conclusion

This study demonstrates that sub-population UPs have the potential to improve head imaging at 7T. Our proof-of-concept results indicate that pTx pulse design based on sub-populations of anatomies reduces SAR variability and improves performance.

References

[1] Le Garrec et al. MRM. 2017. [2] Ball et al. AE. 2011. [3] Shao et al. MRM. 2015. [4] Hoyos-Idrobo et al. IEEE T-MI. 2014. [5] Gras et al. JMR. 2015.

Oral Session 2: Advances in Neuroimaging

Increased Connectivity from Ventral Temporal Cortex to Perisylvian Language Areas During Non-Word Reading – **Vicky He**

Vicky He, Bahman Tahayori, David Vaughan, Graeme Jackson, David Abbott, Chris Tailby, and the Australian Epilepsy Project (AEP)
The Florey Institute of Neuroscience and Mental Health, University of Melbourne

Introduction

Neurobiological models of cognition hold that the degree to which information flows between different brain areas is modulated as a function of cognitive demands[1]. Psychophysiological interaction analysis (PPI) is a regression based method for evaluating such modulations in functional magnetic resonance imaging (fMRI) data[2]. Here we applied PPI methods to investigate the task dependent modulation of connectivity from the Visual Word Form Area (VWFA) during execution of a pseudoword rhyming task. We hypothesised that the VWFA would connect more strongly with perisylvian language areas during pseudoword reading than during a non-language baseline condition.

Methods

One hundred and thirty two AEP participants completed a block design fMRI task contrasting pseudoword rhyming blocks (whether two visually presented non-words would rhyme if pronounced aloud) against visual pattern comparison blocks (whether two patterns composed of forward and backslashes matched). First level analysis was applied using the iBrain toolbox[3] with SPM[4]. The PPI regression includes the main effect of task, the main effect of the seed (VWFA) time course, the interaction between the two, and six head motion parameters. To accurately capture such interaction, it has been suggested to deconvolve the haemodynamic response function (HRF) from the seed time course, multiply it by the task regressor, and then convolve with the HRF[5]. The PPI was implemented using the gPPI (generalised PPI) toolbox[6].

Results

Figure 1 shows the SPM-t image from the second level analysis on the PPI term. There is extensive activation with a peak at the seed location. This indicates a misspecification of the model as the main effect of the seed is included in the regression, and therefore the seed should not appear significant in the interaction. It was suggested by Di and colleagues[7] that this could be due to imperfect deconvolution and convolution of the seed time course, with mean centering the task regressor when forming the interaction proposed as a potential fix. Applying this modification eliminated the diffuse suprathreshold distribution seen in Figure 1, revealing discrete suprathreshold clusters in left posterior temporal and left inferior frontal cortex (Figure 2). The revised results supported our hypothesis that the VWFA connects more strongly with classical language areas during non-word reading.

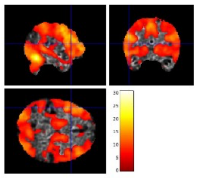

Figure 1

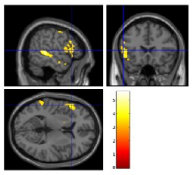

Figure 2

Discussion

Our findings utilising the revised PPI method are consistent with models of the reading system[8] and language[9], as well as the idea of dynamic modulation of information flow according to cognitive demands[1]. Furthermore, the results support the observations of Di and colleagues[7], that with deconvolution, it is essential for the task regressor to be mean centred to avoid spurious results.

Conclusion

Using the revised PPI we found cognitive dependent re-weighting of connections in language-related networks. These results also point to the importance of constructing PPI models appropriately.

References

1] Park & Friston. Science. 2013. 2] Friston et al. NeuroImage. 1997. 3] Abbott & Jackson. NeuroImage. 2001. 4] Friston et al. SPM. 2007. 5] Gitelman et al. NeuroImage. 2003. 6] McLaren et al. NeuroImage. 2012. 7] Di et al. Hum Brain Mapp. 2017. 8] Fiez & Petersen. PNAS. 1998. 9] Hickok & Poeppel. Nat Rev Neurosci. 2007.

Acknowledgements

The AEP received funding from the Australian Government under the Medical Research Future Fund.

Optimising functional brainstem imaging of sympathetic drive with ultra-high field MRI – **Rebecca Glarin**

Rebecca Glarin[1,2], Donggyu Rim[3], Luke A Henderson[4] & Vaughan G Macefield[2,3]
[1]Melbourne Brain Centre Imaging Unit, University of Melbourne; [2] Baker Department of Cardiometabolic Health, University of Melbourne; [3]Baker Heart and Diabetes Institute, Melbourne; [4]Brain and Mind Centre, University of Sydney.

Introduction

Sympathetic outflow is generated within specific nuclei in the brainstem and hypothalamus, with contributions from other subcortical and cortical sites. This outflow is responsible for many regulation processers. Muscle Sympathetic Nerve Activity (MSNA) contributes to the beat-to-beat regulation of blood pressure through its control of arteriolar diameter within the highly vascularised skeletal muscle bed. Skin Sympathetic Nerve Activity (SSNA) contributes to thermoregulation through cutaneous vasoconstriction, vasodilation and sweat release. This activity can be detected as MSNA and SSNA and recorded directly via intraneural microelectrodes. Previously the lab developed the techniques of MSNA-coupled and SSNA-coupled functional magnetic resonance imaging (fMRI), using 3 Tesla MRI. Further extension of this method is being undertaken at Ultra-high field on a 7T MRI. This promises higher spatial resolution, particularly of the brainstem and hypothalamus, than we could previously achieve. We aim to functionally identify the brainstem nuclei responsible for generating sympathetic drive through the use of ultra-high field (7T), high-resolution fMRI coupled with direct recordings of sympathetic nerve activity to muscle and skin.

Methods

Recording procedures: A tungsten microelectrode was inserted percutaneously into a muscle fascicle of the common peroneal nerve at the fibular head of 17 participants (7 MSNA, 10 SSNA). Neural activity was amplified (gain 20 000, bandpass 0.3-5.0 kHz) using a low-noise headstage (NeuroAmpEX, ADInstruments, Australia) and spontaneous bursts of MSNA or SSNA identified and burst amplitudes measured.

Imaging procedures: Blood Oxygen Level Dependent [BOLD] contrast - gradient echo, echo-planar images were collected in the axial plane, on a 7T Magnetom Plus (Siemens Healthcare, Erlangen, Germany) with a 1Tx32Rx channel head coil (Nova Medical, Wilmington, MA, USA). The fMRI sequences are run adopting a 4s-ON, 4s-OFF triggered protocol (Fig 1). This is with consideration of the timing of both neural conduction and central haemodynamic delays and the noise created by the sequence gradients on the nerve signal when recording (Fig 2).

Fig 1. Sequence parameters

Sequence	Nerve Recording	Resolution (mm)	TR (ms)	TE (ms)	Measurements	Bandwidth (Hz/Px)	iPAT	Duration (seconds)
MP2RAGE	-	0.75x0.75.x0.75	5000	2.04	NA	230	4	7:02
Brainstem EPI BOLD	YES	1x1x1	4010	20	210	1608	4	28:52
Whole Brain EPI BOLD	YES	1.2x1.2x1.6	4000	14	150	1582	4	20:52

Fig 3. Brainstem EPI axial acquisition. 1 mm voxels TR=4 s

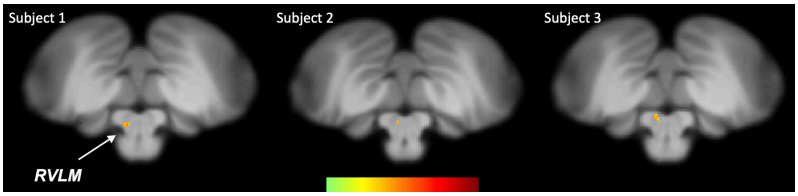

Fig 2. Neural and imaging signal considerations

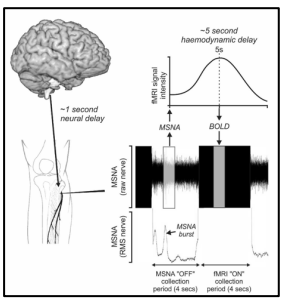

Results

Preliminary analysis has been performed in 3 of 7 successful recordings in healthy participants. In these axial sections MSNA-coupled increases in BOLD activation were detected at the level of the rostral ventrolateral medulla (RVLM) in each participant.

Conclusion

These preliminary results indicate that, using MSNA-coupled fMRI, we can detect increases in BOLD signal intensity in RVLM with 1 mm isotropic voxels. The improved signal to noise and higher resolution available at ultra-high field will allow us to image the small medullary nuclei responsible for generating sympathetic drive with higher precision.

References

Macefield VG & Henderson LA. *NeuroImage.* 2019.

Acknowledgments the facilities, scientific and technical assistance from the National Imaging Facility, a National Collaborative Research Infrastructure Strategy capability, at the Melbourne Brain Centre Imaging Unit, The University of Melbourne. This work was supported by a research collaboration agreement with Siemens Healthineers.

Structure-function relationships in the human hippocampus: new insights using track-weighted dynamic functional connectivity – **Marshall Dalton**

Marshall A. Dalton[1,3], Jinglei Lv[2,3], Arkiev D'Souza[3,4], Fernando Calamante[2,3,5]
[1]School of Psychology, Faculty of Science, University of Sydney, Australia
[2] School of Biomedical Engineering, Faculty of Engineering, University of Sydney, Australia
[3]Brain and Mind Centre, University of Sydney, Australia
[4]Translational Research Collective, Faculty of Medicine and Health, The University of Sydney, Australia
[5]Sydney Imaging, University of Sydney, Australia

Introduction

The hippocampus is a brain structure that is critical for healthy memory function[1]. Recent technical and methodological advances have allowed us to conduct increasingly detailed investigations of structural connectivity (SC) and functional connectivity (FC) of the human hippocampus in-vivo using MRI. However, SC and FC of the human hippocampus are most often analysed independently, thereby limiting our ability to understand structure-function relationships of cortico-hippocampal connectivity in the human brain. To address this gap, we investigated the relationship between SC and FC of the human hippocampus using track-weighted dynamic functional connectivity (TW-dFC) mapping[2].

Methods

In brief, we leveraged TW-dFC to fuse SC and dynamic FC data into a quantitative 4D image (i.e., with spatial+temporal information), which was used to characterise structure-function relationships. Ten subjects were selected from the HCP 100 unrelated subject database. For each subject, we used DWI data to generate SIFT2-weighted whole-brain streamlines and isolate only those connecting the hippocampus with the rest of the brain ('hippocampus tractogram') using methods described elsewhere[3]. We calculated the TW-dFC map for the hippocampus tractogram by assigning each streamline a 'dynamic functional weighting' given by the (sliding window) functional correlation between resting state BOLD fMRI data at its end-points[2]. In essence, this method projects grey matter functional connectivity information to the intersecting white matter pathways. TW-dFC maps were computed and the TW-dFC data were further analysed using independent component analysis (ICA; using FSL MELODIC software[4]). The ICA results were used to identify clusters within the hippocampus based on the time-series associated with each hippocampal endpoint in the TW-dFC maps. In essence, this allowed us to characterise, in a data-driven manner, spatially distinct functional clusters along the anterior-posterior axis of the hippocampus and identify the distinct cortical networks associated with each functional cluster.

Results

Our method was effective in identifying differentiable functional clusters within the human hippocampus. The results of ICA revealed multiple functional clusters along the anterior-posterior and medial-lateral axes of the hippocampus. Each cluster was functionally associated with different cortical areas. Group level analysis confirmed that separate functional clusters within the hippocampus were associated with different cortical networks, each associated with their own dynamic functional fingerprint.

Discussion

Our results revealed how specific regions within the human hippocampus display anatomical and dynamic functional connectivity with distinct cortical areas. We found strong functional associations between the posterior hippocampus and medial parietal regions and, in contrast, between the anterior hippocampus and temporal brain areas. Strikingly, different functional clusters within the hippocampus displayed distinct patterns of cortical connectivity. For example, separate clusters in the hippocampus displayed preferential dynamic functional connectivity with medial parietal, occipital and temporal areas. Taken together, these observations provide new detailed insights into structure-function relationships within the human hippocampus and have important implications for theories of human hippocampal function along its anterior-posterior axis[5].

Conclusion

Mapping structure-function relationships in the human hippocampus will help us develop more detailed and integrated models of human memory and its biological basis. Overall, our results contribute to ongoing efforts to characterise the relationship between human hippocampal SC and FC with implications for understanding hippocampal function in health and dysfunction in disease.

References

[1] Maguire et al. J Exp Psychol Gen, 142(4): 1180-1189, 2013. [2] Calamante et al. Brain Struct Funct, 222(8): 3761-3774, 2017. [3] Dalton et al. eLife, In Press, 2022. [4] Smith et al. NeuroImage, 23(1): S208-S219, 2004. [5] Poppenk et al. Trends Cogn Sci, 17(5): 230-40, 2013.

In vivo microstructural border delineation between areas of the human cerebral cortex using magnetic resonance fingerprinting (MRF) residuals – **Shahrzad Moinian**

***Shahrzad Moinian*[1,2], *Viktor Vegh*[1,2], *David Reutens*[1,2]**

[1]ARC training Centre for Innovation in Biomedical Imaging Technology, The University of Queensland, Brisbane, Australia, [2]Centre for Advanced Imaging, The University of Queensland, Brisbane, Australia

Introduction

The current in vivo MRI resolution is several orders of magnitude larger than the scale of microstructural components in the brain tissue, requiring costly multi-contrast image acquisition and complex models for inferring microstructural features from in vivo MRI.[1] We previously demonstrated that spatiotemporal MR fingerprinting[2] residual signals[3] contain rich descriptive area-specific representation for each voxel, leading to the development of a machine learning model for in vivo cortical parcellation.[3] The study relied on a brain atlas[4] to provide probabilistic masks of cortical regions to label the training samples. Here, we investigated the utility of area-specific information in MRF residuals to develop an automated atlas-free analysis pipeline for in vivo cortical border delineation in individuals.

Methods

We acquired 3D EPI-MRF scans from six healthy participants aged 31±4 years using a 7T MR scanner (Siemens Healthcare, Erlangen, Germany), and calculated MRF residual signal and the corresponding autocorrelation profile per voxel, as detailed previously.[3] Our basis was that the differences between MRF residual signals would be smaller for voxels which are located in a single cortical region, compared to those across microstructurally different cortical borders. A total of 300 2D paths along the cortical ribbon in each individual scan were extracted from sagittal (see figure 1a), coronal and axial slices of 3D MRF images from six participants, using the Juelich maximum probability map of cortical areas.[4] For each voxel along the path, we created a 3x3 2D kernel surrounding the voxel of interest, excluding the non-GM tissue. We then measured the average Euclidean distance (ED) between the MRF residual signal of the centre voxel and all other kernel voxels as we traversed each path. The ED values outside two standard deviations from the mean distance values from each distance profile were considered as the peak distance values. The spatial location of the voxels corresponding to the peak ED values were examined to see if they were located within a 2-voxel radius from the border between any two cortical areas on the Juelich maximum probability map of the participant.

Results and discussion

Figure 1a depicts an example path crossing the premotor area BA6 and primary motor areas BA4p and BA4a overlayed on an MRF scan from one participant, with residual distance profile for the path in Figure 1b. As an example, the spatial location of three of these peak voxels on the Juelich maximum probability map of the individual is illustrated in Figures 1c-e. We found that the first peak (at path indices 122-123 in Figure 3c) corresponds to the border between areas BA6 and BA4p. Additionally, the second (at path indices 134-15 in Figure 1d) and third (at path indices 141-13 in Figure 3e) peaks correspond to the border between BA4a and BA4p and between BA6 and BA4a, respectively. Across all participants, we observed that 90% of the border voxels detected were located at the 2-voxel radius of

the border between two areas on the Juelich maximum probability map. The co-localisation of the peak ED values on the MRF residual distance profiles and the border voxels on the Juelich maximum probability map suggests the presence of microstructural information in the MRF residual signals, providing a tool for accurate in vivo voxel-wise cortical parcellation in individuals.

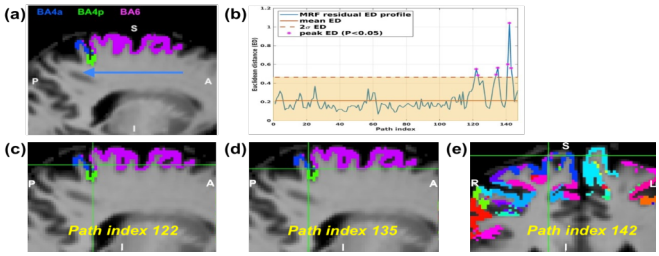

Figure 1. (a) An example sagittal path crossing through premotor area BA6 and primary motor areas BA4a and BA4p. The blue arrow shows direction of travel through the path. (b) The MRF residual distance profile along this path with the peak Euclidean distance (ED) values indicated by the asterisks. (c-e) The voxel locations corresponding to the peak ED values at path indices 122, 135 and 142, respectively, indicated by the crosshairs on the participant's cerebral cortex maximum probability map.

Conclusion

Using MRF residual signals we demonstrated the feasibility of developing an automatic atlas-free border delineation between microstructurally distinct regions of the human cerebral cortex in vivo. This study sets the foundation for future work to develop robust unsupervised machine learning-based in vivo cortical parcellation in individuals.

References

[1] Cercignani & Bouyagoub. Neuroimage. 2018. [2] Ma et al. Nature. 2013. [3] Moinian et al. Cerebral Cortex. 2022. [4] Amunts et al. Science. 2020.

Data-driven in-vivo parcellation of human subcortex – **Tonima Ali**

Tonima S. Ali[1,2], Jinglei Lv[1,2], Marshall Dalton[2,3], Steve Kassem[4], Arkiev D'Souza[1,2,5], Fernando Calamante[1,2,6]

Affiliations: 1. School of Biomedical Engineering, The University of Sydney; 2. Brain and Mind Centre, The University of Sydney; 3. School of Psychology, The University of Sydney; Neuroscience Research Australia, 5. Translational Research Collective, The University of Sydney. 6. Sydney Imaging, The University of Sydney.

Introduction: Human subcortex comprises multiple deep grey matter (DGM) structures, many with several nuclei and specialised sub-regions dedicated to highly specific functions. Detailed knowledge on the anatomy and topography of these regions are fundamental to understanding the integrative connectivity patterns within DGM structures and to map the specialised cortico-DGM circuits. Histologydriven brain atlases[1–3] provide detailed delineation of these sub-regions, however, those cannot be directly applied to *in-vivo* MRI studies. Here, we integrate the information from anatomy, diffusion microenvironment, and directions of white matter (WM) fibres within DGM, from multi-contrast MRI, to segregate the nuclei and specialised sub-regions of DGM structures in a normal population leading towards the delineation of specialised brain networks.

Methods: Minimally pre-processed T1w, T2w, and Diffusion MRI (dMRI) data obtained at 3T were downloaded from Human Connectome Project[4–6] for 10 healthy subjects. For each subject, fractional anisotropy (FA), mean diffusivity (MD), axial diffusivity (AD), radial diffusivity (RD), and myelin index (T1w/T2w) were computed following the processing pipeline in [7]. Additionally, orientation of the dominant WM fibre tracts were computed within each voxel[8]. 20 million streamlines were generated and the volumetric maps were combined by computing track-weighted imaging maps[9] with 0.7mm isotropic super-resolution[9]. Parametric maps were warped to a tissue-unbiased template[10] and DGM regions were defined using FastSurfer[11,12]. Components contributing to >5% of the total variance of the combined dataset were identified by principal component analysis, and hierarchical k-means clustering was employed on the principal components to segregate the sub-regions within each DGM structure.

Results and Discussions: Figure 1 show an example of parcellated DGM structures (a, c) next to delineations from human brain atlas[1] (b, d) at equivalent coronal planes, illustrating the parcellations for caudate, putamen, globus pallidus, nucleus accumbens, and thalamus. The resemblance between (a, c) and (b, d) is clearly visible at both locations. Focusing only on putamen (outlined) for brevity, arrows show sub-regions coloured in pink, blue and orange that correspond to the fundus of the putamen, the putamen, and the 'external putamen', respectively. The first two sub-structures have distinct neuroanatomy and are recognised as specialised sub-regions within putamen[1]. Of particular note, our data driven approach also identified the 'external putamen', a region which has only recently been identified by neuroanatomists as having distinct anatomical and functional properties[13,14] and is yet to be added to extant human brain atlases.

These results provide evidence that each of the specialised subregions of DGM structures are discernible by unique combination of diffusion properties, WM fibre orientations, and myelin content specific to that region. Additionally, our multi-contrast MRI analysis is sensitive to these attributes and can segregate these regions exclusively from the MRI-derived data without any functional or anatomical prior. Tian et al. has recently demonstrated the topographic organisation of human subcortex using MRI-driven functional connectivity gradients[15]. Our results show similarities to the major clusters obtained by this work, when WM fibre orientation is incorporated. However, the use of TW imaging maps has substantially increased the resolution of our data, which has enabled the identification of many smaller regions within DGM structures, fundus of the putamen for example, which were not identifiable by previous MRI-based parcellations.

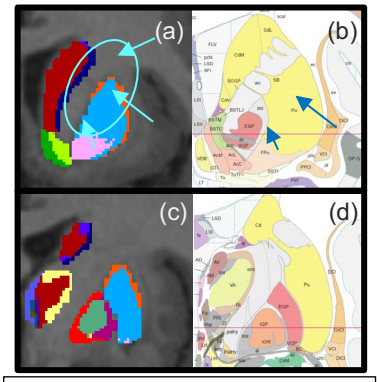

Figure 1: Multi-contrast MRI data-driven parcellation (a, c) next to sections (b, d) from human brain atlas[1] at equivalent coronal planes

Conclusion: This study aims to develop a publicly available MRI data-driven parcellation of human subcortex. Our detailed delineation of the specialised sub-regions within DGM structures can be directly applied to subject-specific and/or group average MRI dataset. The findings from this work may improve the overall understanding of DGM sub-structures *in-vivo*, the specialised brain networks involving DGM, and allow connectome analysis with higher specificity.

References: [1] Mai et al. Trends Neurosci. 2010.[2] Shen at al. Trends Neurosci. 2010. [3] Eugenio et al. Neuroimage. 2010. [4] Van Essen et al. Neuroimage. 2013. [5] Sotiropoulos et al. Neuroimage. 2013. [6] Glasser at al. Neoroimage. 2013. [7] Ali et al. Magn Reson MRI. 2022. [8] Ali et al. Proc ISMRM. 2020. [9] Calamante et al. Neuroimage. 2011. [10] Lv et al. Biorxiv. 2022. [11] Henschel et al. Neuroimage. 2020. [12] Patenaude 2t al. Neuroimage. 2011. [13] Mehlman et al. J Neurophysiol. 2019. [14] Devan et al. *Neurobiol Learn Mem*. 2011. [15] Tian et al. Nat Neurosci. 2020.

Oral Session 3: Clinical applications of advanced MRI

Quantitative MRI: defining measurement uncertainty for detecting treatment response in longitudinal imaging of prostate cancer – **Yu-Feng Wang**

***Yu-Feng Wang*[1,2], *Sirisha Tadimalla*[1,3], *Yu Sun*[1], *Lois Holloway*[1,2,4], *Annette Haworth*[1]**

1 Institute of Medical Physics, School of Physics, Faculty of Science, The University of Sydney, Sydney

2 Ingham Institute for Applied Medical Research, Sydney

3 Sydney West Radiation Oncology, Westmead Hospital, Sydney

[4]South Western Sydney Clinical School, University of New South Wales, Liverpool, NSW, Australia

Introduction

Prostate cancer (PCa) is the most commonly diagnosed cancer among males in Australia. [1] Recurrence of PCa following radiation therapy is not uncommon but can be treated with salvage therapies if detected prior to development of metastases. The current standard of care post-treatment monitoring involves measurement of prostate specific antigen levels in blood serum, which lacks accuracy and specificity in detecting recurrent disease. [2] Quantitative MRI (qMRI) parameters have shown potential for providing non-invasive imaging biomarkers of treatment response and may enable early detection of recurrent PCa. [3, 4] Measurement uncertainties in the qMRI parameters, however, could impact the reliability to detect treatment-related changes. [5] An in vivo test-retest study was therefore conducted with the aim to establish thresholds for reliable detection of treatment-related changes in longitudinal monitoring of prostate cancer with qMRI.

Methods

Test-retest images were acquired in 9 Ca patients and 6 healthy volunteers on two 3T MRI scanners (Prisma and Skyra, Siemens Healthineers, Erlangen, Germany). The apparent diffusion coefficient (ADC), diffusion (D), perfusion fraction (f), hypoxia score (HS), T1, pharmacokinetic modelling of dynamic contrast enhanced (DCE) MRI and R2* parametric maps were obtained. Radiomic features were extracted from T2w images and the qMRI parameter maps. The repeatability coefficient (%RC) was calculated for region of interest (ROI) and voxel-wise measurements of the parametric maps in the tumour and benign tissues in the peripheral and non-peripheral (PZ and nPZ) prostate zones. The repeatability of DCE-derived qMRI parameters was estimated by propagation of uncertainties in T1.

Results

The %RC of ADC, D, HS and their radiomic features were significantly different between the PZ and nPZ (two-tailed t-test $p<0.05$) and also between tumour and benign tissue types ($p<0.05$). The %RC of *f*, T1, R2* and their radiomic features were not significantly different between anatomical zones and between tumour and benign tissue types. DCE-derived qMRI parameters and T1 had relatively lower %RC than DWI-derived parameters and R2* (range from 0.8% to 10.5% compared to 4.7% to 40.0% for ROI measurements). Measurement uncertainties were larger when test-retest variations were assessed using voxel-wise analysis compared to the ROI measurements.

Discussion

The uncertainty of qMRI parameters derived from DWI (all except f) was found to be higher in the PZ, likely due to the closer proximity to the rectum and vulnerability to rectal gas-induced artefacts. The higher uncertainty of ADC and D in the tumour compared to benign tissues was likely due to the smaller ROI size. In comparison to the ROI-based approach, the higher uncertainties in voxel-wise measurements of parametric and feature maps, likely due to lower SNR and image registration, could be a challenge in mapping of treatment response.

Conclusion

Thresholds of change required to distinguish true treatment-related changes from measurement uncertainties can be formulated for the qMRI parameters, however these thresholds should be defined separately for anatomical zones and tissue types for DWI-derived parameters and features. The remaining qMRI parameters and features can have a single threshold measured from the whole prostate. DCE-derived qMRI parameters and T1 have relatively higher precision and could potentially be more reliable in detecting treatment-related changes. The thresholds established in this study can enable discrimination of true treatment-related changes from measurement uncertainties in future longitudinal imaging studies to develop robust quantitative imaging biomarkers of treatment response.

Acknowledgements

This project was supported by NHMRC grant APP1126955, Sydney West TCRC – Partner Program 2019 and CI NSW Translational Program Grant TPG182165.

References

1. Health et al. Canberra. 2021
2. Vicini et al. J Urol. 2005
3. Sun et al. Australas Phys Eng Sci Med. 2019
4. Wang et al. J Med Imaging Radiat Oncol. 2021
5. Shukla-Dave et al. J Magn Reson Imaging. 2019

Leukoencephalopathic changes after treatment for breast cancer and their association with serum neurofilament – **Gwen Schroyen**

Gwen Schroyen[1,2,3], Charlotte Sleurs[1,2,4,5], Tine Ottenbourgs[3], Nicolas Leenaerts[1,6,7,8], Michelle Melis[1,2,3], Ann Smeets[2,5,9], Sabine Deprez[1,2,3], Stefan Sunaert[1,3,10]

1) KU Leuven, Leuven Brain Institute, Leuven, Belgium
2) University Hospitals Leuven, Leuven Cancer Institute, Leuven, Belgium
3) KU Leuven, Department of Imaging and Pathology, Translational MRI, Leuven, Belgium
4) Tilburg University, Department of Cognitive Neuropsychology, Tilburg, The Netherlands
5) KU Leuven, Department of Oncology, Leuven, Belgium
6) KU Leuven, Department of Neurosciences, Mind-Body Research, Leuven, Belgium
7) KU Leuven, University Psychiatric Center, Leuven, Belgium
8) University Hospitals Leuven, Department of Psychiatry, Leuven, Belgium
9) University Hospitals Leuven, Department of Oncology, Surgical Oncology, Leuven, Belgium
10) University Hospitals Leuven, Department of Radiology, Leuven, Belgium

Introduction

Earlier case-studies[1] have provided evidence of chemotherapy-induced leukoencephalopathy in patients with breast cancer, but prospective research is missing. We investigated leukoencephalopathy pre- and post-chemotherapy and its association with a serum neuroaxonal damage marker.

Methods

This prospective cohort study included 40 patients receiving chemotherapy for non-metastatic breast cancer, as well as 39 chemotherapy-naïve patients and 40 healthy women age- and education matched (32-64 years of age), from 2018-2021. Data acquisition included fluid-attenuated inversion-recovery (FLAIR; 183 sagittal slices, voxel size = 1 mm isotropic, TR/TE = 4800/340 ms, FA = 40°, FOV=256×256, number of signals averaging NSA = 2)) magnetic resonance imaging (MRI) on a 3T Philips Achieva system (32-channel phased-array head coil) for lesion volumes[2,3] (total, juxtacortical, periventricular, infratentorial and deep white matter) and serum neurofilament light chain (sNfL) before, three months- and one-year post-chemotherapy, or at matched timepoints. Differences between groups in changes throughout time were compared using robust mixed-effects modelling and associations between total lesion volume and sNfL were analysed using linear regression.

Results

Stronger increases in periventricular and deep white matter lesion volumes were observed shortly post-chemotherapy compared to chemotherapy-naïve patients and in the deep white matter compared to healthy women. A stronger increase in sNfL concentration was observed shortly post-chemotherapy compared to both control groups, showing stable levels for both time-points, while a decrease was observed compared to healthy women one-year post-chemotherapy. sNfL concentrations measured shortly or one-year post-chemotherapy were associated with lesion volume one-year post-chemotherapy (or at matched time intervals), while baseline levels or changes were not.

Discussion

This was the first prospective study to evaluate changes in leukoencephalopathy and neuroaxonal damage, as measured with NfL, in patients treated for non-metastatic breast

cancer. These results underscore the possibility of chemotherapy-induced leukoencephalopathy several months post-treatment, as well as the potential of sNfL as a prognostic marker for peripheral/central neurotoxicity, such as the observed leukoencephalopathy.

Conclusion

Future studies evaluating the association between serum NfL, lesion load, and cognitive impairment will be critical in elucidating neurocognitive impairments after cancer therapy.

References

1) Ferguson. J. Clin Oncol. 2007.
2) Jain et al. Neuroimage. 2015.
3) Rakić et al. Neuroimage Clin. 2021.

Early identification of cerebral small vessel disease in obstructive sleep apnoea patients using magnetic resonance spectroscopy: a pilot study – **Arunan Srirengan**

***A. Srirengan*[1], *K. Lancaster*[2], *L. Bilston*[1,2], *E. Brown*[2,3], *C. Rae*[1,2], *L. Cysique*[1,4], *L. Jugé*[1,2]**

[1.] University of New South Wales, [2.] Neuroscience Research Australia, [3.] Prince of Wales Hospital, [4.] St Vincent's Hospital

Introduction. Cerebral small vessel disease (CSVD) is an incurable, slowly progressing disease that affects the small vessels in the brain and can lead to cognitive impairment and dementia later in life[1]. Obstructive sleep apnoea (OSA)[2], a common sleep-breathing disorder, is an under-recognised cause of CSVD. The diagnosis and monitoring of CSVD rely on imaging findings[1]. However, only severe cases of CSVD in moderate-severe OSA patients can be identified with conventional MRI protocols[3]. Thus, we proposed to determine whether proton MR spectroscopy (^{1}H MRS) can assist in identifying earlystage CSVD in patients with OSA by quantifying brain metabolites associated with neuronal integrity (N-acetylaspartate (NAA)), membrane metabolism (glycerophosphocholine (GPC)), energy metabolism (creatine (Cr)), neurotransmitter activity (glutamate (Glu)) and glial cell inflammation (myo-inositol (mI))[4]**.**

Methods. Fourteen participants (11 women, 46–64 years) underwent brain MRI (Philips Achieva 3TX). Five participants had no OSA [apnoea hypopnoea index (AHI) < 10 events/hr sleep], and nine patients matched for age and BMI had untreated OSA [AHI ≥ 10 events/hr sleep]. T1-weighted and FLAIR anatomical scans were qualitatively analysed using STRIVE criteria[5], with each participant receiving a STRIVE CSVD score based on the presence of four imaging markers of CSVD (white matter hyperintensities (WMH), cerebral microbleeds, silent brain infarction and enlarged perivascular spaces).^{1}H MRS was obtained from the prefrontal cortex and frontal periventricular white matter to quantify brain metabolite concentrations with reference to water using jMRUI V.4. Pearson correlation evaluated the relationship between variables, while Mann-Whitney U tests assessed differences between groups.

Results. One or more STRIVE CSVD features were present in similar proportions of controls (2/5) and OSA patients (5/9). STRIVE CSVD score did not differ between groups (OSA: 0.6±0.5, controls: 0.4±0.5; p>0.99), nor did WMH volume and count (p=0.52 and p=0.50, respectively), suggesting earlystage CSVD in both OSA and control groups. In the prefrontal cortex, higher AHI was associated with increased GPC/H_2O (r=0.60, 95% CI [0.01 to 0.88]), NAA/H_2O (r=0.64, 95% CI [0.06 to 0.90]) and ml/H_2O ratios (r=0.70, 95% CI [0.16 to 0.91]), but not with Glu/H_2O or Cr/H_2O. Amongst OSA patients, there were no significant differences in metabolite concentrations between participants with and without STRIVE CSVD imaging features, in either prefrontal cortex or frontal periventricular white matter.

Discussion. Abnormal prefrontal cortex metabolites may indicate early OSA-related CSVD injury, with elevated GPC and mI levels reflecting increased membrane turnover and the presence of neuroinflammation. Results demonstrate that mild to severe OSA contributes to

the pathogenesis of CSVD. The absence of difference in metabolite concentrations between participants with and without STRIVE CSVD imaging features suggest that abnormally elevated metabolic concentration is also commonly seen in in OSA patients without imaging features and could be an early indicator of neurovascular injury not captured by conventional MRI protocol.

Conclusion. The preliminary findings of this ongoing study support the use of brain MR spectroscopy to complement conventional MRI protocol for diagnosing early-stage CSVD, and reinforce the need for early intervention in OSA.

References

1] Shi et al. Stroke Vasc Neurol. 2016.
2] Motamedi et al. Ochsner J. 2009.
3] Huang et al. Sleep. 2020.
4] Rae, C.D. Neurochem Res. 2014.
5] Wardlaw et al. Lancet Neurol. 2013.

Acknowledgements

This study was supported by the Brain Foundation and the UNSW Ageing Futures institute.

Hippocampal Glx in RRMS: A potential therapeutic indicator in fingolimod and injectables – **Oun Al-iedani**

***Oun Al-iedani*[1,2], *Rodney Lea*[2,3], *Saadallah Ramadan*[2,4], *Vicki E. Maltby*[2,5,6], *Jeannette Lechner-Scott*[2,5,6]**

[1]School of Biomedical Sciences and Pharmacy, College of Health, Medicine and Wellbeing, University of Newcastle, NSW, Australia. [2]Hunter Medical Research Institute, New Lambton, NSW, Australia. [3]Institute of Health and Biomedical Innovation, School of Biomedical Sciences, Queensland University of Technology, Brisbane, Australia. [4]School of Health Sciences, College of Health, Medicine and Wellbeing, University of Newcastle, NSW, Australia. [5]School of Medicine and Public Health, College of Health, Medicine and Wellbeing, University of Newcastle, NSW, Australia. [6]Department of Neurology, John Hunter Hospital, New Lambton Heights, NSW, Australia.

Introduction

Disease-modifying therapies (DMTs) can reduce relapses and mitigate the long-term damage in people with relapse-remitting MS (pw-RRMS)[1]. Magnetic resonance spectroscopic (MRS) studies have shown a positive effect of DMT on neurometabolites in pw-RRMS, which correlates with maintaining axonal metabolic function[2]. Hippocampal demyelination and dysregulation of a major excitatory neurotransmitter (glutamate+glutamine; Glx) are associated with memory impairment in pw-RRMS[3]. To date, evaluating the longitudinal DMT effect on hippocampal metabolism in pw-RRMS has not been investigated.

Methods

A total of 65 pw-RRMS on fingolimod (N=36) or injectable (glatiramer acetate (GA) or interferon (IFN), N=29), were age and sex matched to HCs (N=44). All MRI and hippocampal MRS (voxel size=30x15x15mm3)(Fig.1) were acquired from pw-RRMS and HCs cohorts at baseline and 2 years follow-up. Segmentation of brain MRI/S was performed by FSL/SPM12. All pw-RRMS underwent cognitive, fatigue and mental health assessment as well as Expanded Disability Status Scale (EDSS).

Results

Pre- and post-mean hippocampal Glx levels were significantly altered in the MS cohorts ($p \leq 0.05$): fingolimod (1.47±0.51 vs 1.06±0.39) and injectable (1.33±0.06 vs 1.16±0.04) but HCs remained stable (1.161±0.46 vs 1.158±0.35). However, post-hoc tests revealed fingolimod is associated with a larger statistically significant reduction in hippocampal Glx($p=0.003$) compared to injectable($p=0.01$) and a trend to be lower compared to HCs($p=0.09$)(Fig.2). Hippocampal NAA levels showed statistically significant increase in fingolimod cohort ($p \leq 0.0001$) compared to HCs over the 2-yrs follow-up(Fig.3).

Discussion

The current study is the first longitudinal in-vivo investigation comparing the impact of fingolimod, IFN-b or GA on the hippocampal metabolism in RRMS patients. Glx plays a critical role in important metabolic functions including oxidative energy supply to neurons/astrocytes and production of GABA. Excessive Glx can lead to neurotoxicity, neurodegeneration, and dysfunction in the glutamatergic pathway in addition to abnormal neuronal signalling.

Conclusion

Fingolimod has a stronger impact on hippocampal Glx and NAA brain profiles than injectable DMTs. Our results suggest that MRS might be used as a therapeutic indicator.

References

1. Hutchinson M. Ther Clin Risk Manag 2007. 2. Yetkin MF, et al. Medicine (Baltimore) 2016.
3. Muhlert N, et al. Journal of neurology, neurosurgery, and psychiatry 2014.

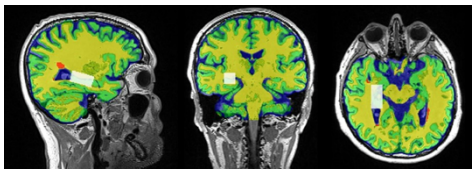

Fig.1. T1-MR images in 3 planes demonstrating the hippocampal voxel size and position (white box) and tissue segmentation (WM-yellow, GM-green and CSF-blue and lesion in red).

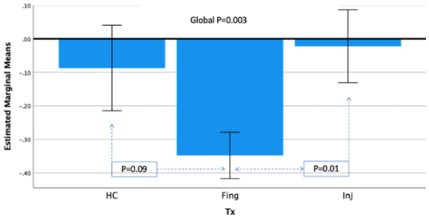

Fig.2. The comparison of hippocampal Glx levels in RRMS treatments cohorts (fingolimod and injectable) and HCs group

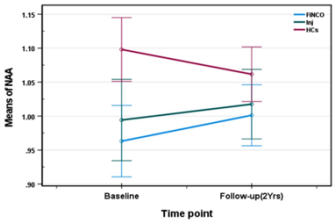

Fig.3. The comparison of hippocampal NAA levels in RRMS treatment cohorts (fingolimod and injectable) and HCs group over 2time points (baseline and 2yrs follow-up).

Personalised quantitative susceptibility mapping in the identification of traumatic brain injury neurodegeneration – **Karen Caeyenberghs**

Juan F Domínguez D[1], Ashley Stewart[2], Alex Burmester[1], Jake Burnett[1], Adam Clemente[3], Phoebe Imms[4] , Hamed Akhlaghi[5], Steffen Bollmann[2] and Karen Caeyenberghs[1]

[1]Cognitive Neuroscience Unit, School of Psychology, Deakin University, Geelong, Australia; [2]School of Information Technology and Electrical Engineering, The University of Queensland, Brisbane, Australia
[3]Healthy Brain and Mind Research Centre, School of Behavioural, Health and Human Sciences, Faculty of Health Sciences, Australian Catholic University, Melbourne, Australia; [4]University of Southern California, Leonard Davis School of Gerontology, Los Angeles, United States; [5]Department of Medicine, St. Vincent's Hospital, Melbourne, Australia

Introduction: Emerging evidence suggests that traumatic brain injury (TBI) is a major risk factor for developing neurodegenerative disease later in life. Recently, quantitative susceptibility mapping (QSM) has been shown to be a promising tool in the investigation of iron concentration in neurodegenerative diseases. QSM has been used by an increasing number of studies in investigations of pathophysiological changes in mild TBI [1]. However, very few clinical QSM studies have been conducted so far. In the present study, we examined changes in magnetic susceptibility in moderate-to-severe TBI patients, to better characterize the underlying mechanisms of neurodegeneration at the level of individual patients.

Methods: Chronic moderate-severe TBI patients (N=4) and healthy controls (N=12) underwent QSM (multi-echo), and anatomical MRI (MPRAGE, voxel size = 0.8mm isotropic) on a 3T Siemens PRISMA scanner. Using the fully automated QSMxT framework [2], we reconstructed the multi-echo susceptibility maps using two-pass QSM. We extracted values of magnetic susceptibility in grey matter regions across the whole brain and determined if they clinically deviated from a reference healthy control group [Z-score < -3.29 or > 3.29 , relative to the control mean].

Results: Our findings revealed that each TBI patient had a unique pattern of clinically significant changes in magnetic susceptibility. These changes included both increases and decreases in magnetic susceptibility. For example, one patient had an increase in magnetic susceptibility in the right inferior frontal and paracentral gyri but a decrease in the right frontal pole. Another patient exhibited decrease in magnetic susceptibility only, in a network of areas including the temporal pole and precentral and lingual gyri on the left, and supramarginal and inferior frontal gyri on the right (see Figure 1).

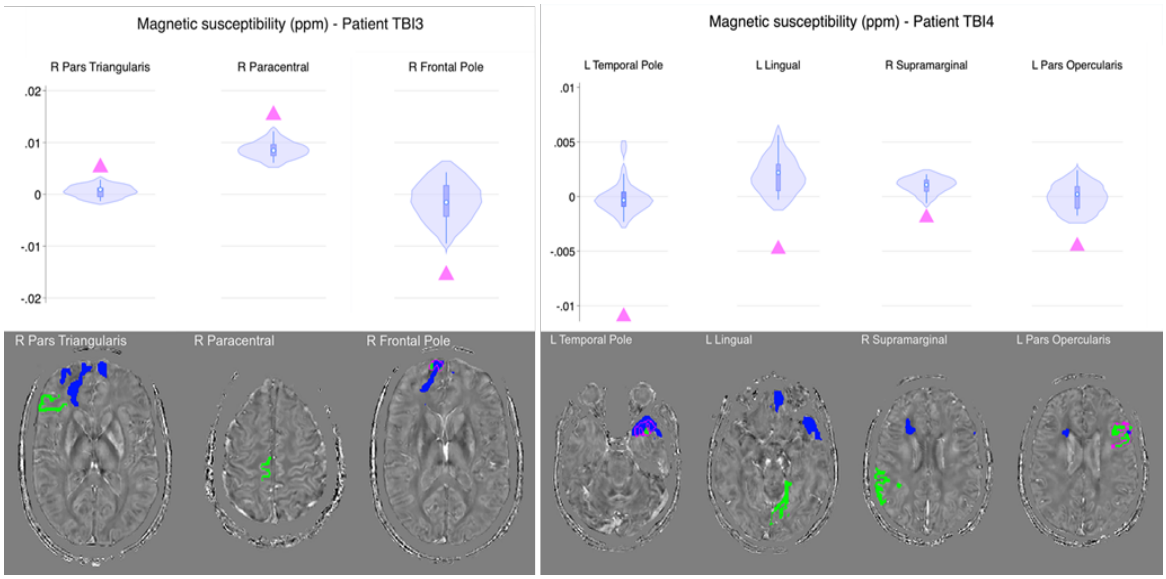

Figure 1. Brain regions with substantial changes in magnetic susceptibility in TBI patients [Z-score <> ±3.29 relative to the control mean]. **Top**: Violin plots showing the distribution of magnetic susceptibility measures in the control sample, with the magenta triangles ▲ indicating the measures of the selected region in the patient. **Bottom**: the sampled areas are depicted in green. Magenta outline (if present) reveals portion of region resected by a lesion (not sampled). The lesion (if present/visible) appears in blue. L, left; R, right.

Discussion & Conclusion:

Our findings in GM susceptibility values in the chronic phase of injury may reflect alterations in iron and calcium deposition. Personalised quantitative susceptibility mapping may be used by clinicians, in the future, to formulate a neuroscience-guided integrative rehabilitation program for TBI patients based on their unique lesion load and individual QSM profile, together with profiles from other neuroimaging (diffusion or volume) and behavioural (cognitive or affective) domains.

References: [1] Gozt A, et al. Neuroscience. 2021 Jul 15;467:218-236. [2] Stewart AW, et al. Magn Reson Med. 2022 Mar;87(3):1289-1300

ECR Data Blitz Session

Deep learning-based mutual and modality-specific information disentanglement of MR and PET for low-dose PET image processing robust to varying levels of dose reduction – **Cameron Pain**

Cameron Dennis Pain[12], Gary Egan[13], Zhaolin Chen[14]

[1]Monash Biomedical Imaging, Monash University, Melbourne, Australia,
[2]Department of Electrical and Computer Systems Engineering, Monash University, Melbourne, Australia
[3]Turner Institute for Brain and Mental Health, Monash University, Melbourne, Australia
[4]Department of Data Science and AI, Monash University, Melbourne, Australia

Introduction

Deep learning has shown potential to facilitate significant dose-reduction factors in MR-PET imaging. Clinical application of these methods is limited by the reliability when applied to data outside the distribution of training data. This work presents a deep learning-based method which leverages reliable information from MR images for consistent performance on PET images acquired at varying dose levels.

Methods

A disentangled latent space representation as shown in figure 1 is used to separate information into MR-PET mutual features and PET specific features, which are mixed and mapped to standard-dose PET. A total of 28 F18-FDG PET brain images were used for training (22), validation (2) and testing (4). Low-dose PET data at x2 and x100 dose reduction (DR) was synthesised by Poisson resampling of the standard dose sinograms. The proposed network architecture and a Unet[1] were trained to map x2 low-dose PET to standard-dose PET and tested on x2 and x100 low-dose data. The total loss function for the proposed architecture is defined as

$$L_{total} = l_z L_z + l_\lambda L_\lambda + l_\Lambda L_\Lambda + l_f L_f$$

Where L_z and L_λ are L2 data consistency, L_Λ constrains the amount of PET information allowed through the network, L_f is mutual feature consistency between PET and MR, and $l_z, l_\lambda, l_\Lambda, l_f$ are set to $1.0, 1.0, 3.0$ and 10.0 respectively. Image quality was evaluated using SSIM[2] and PSNR, and quantitative accuracy was evaluated using relative absolute error.

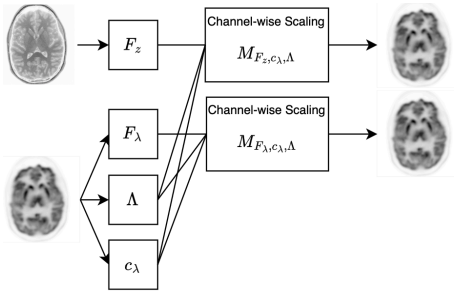

Figure 3: Mutual features F_z and F_λ are extracted from MR and PET respectively, while PET specific features Λ and c_λ are extracted from PET.

Results

Figure 2 shows standard dose images synthesised with the proposed architecture and with the reference Unet at x2 and x100 DR inputs and the spatial distribution of relative absolute error. SSIM and PSNR of reconstructed images at x2 DR and x100 DR are (0.92,32.42) and (0.88,30.12) for the proposed architecture, and (0.96, 36.12) and (0.76,23.3) for the Unet.

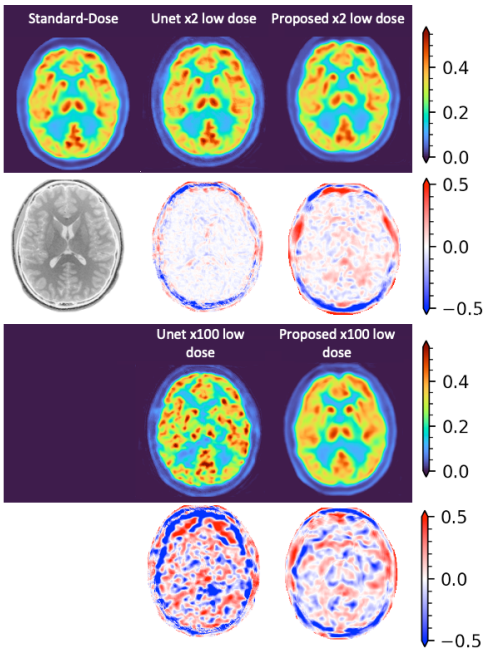

Figure 4: Low-dose to standard-dose mapping for x2 low-dose PET and previously unseen x100 low-dose PET for the proposed architecture and a Unet.

Discussion

The proposed architecture performs consistently on x2 DR data and previously unseen x100 DR data at the cost of degraded performance on in-distribution data. The proposed method in combination with standard-supervised training provides a means of maximising performance in distribution whilst providing robust performance on outlier cases with significantly further reduced dose. The utility of the proposed method is also predicated on MR images being reliably consistent with those used in training.

Conclusion

The proposed method provides consistent performance on x2 DR and previously unseen x100 DR PET images, providing a means of reliably handling outlier cases of further reduced dose.

References

[1]Ronneberger et al., MICCAI 2015.
[2]Wang et al., IEEE Trans. Image Process., 2004

3D Basis Encoded Excitation (3DBEE) – **Negin Yaghmaie**

Negin Yaghmaie[1, 2], Warda Syeda[3], Yasmin Blunck[1, 2], Bradford Moffat[1], Rebecca Glarin[1, 4], and Leigh A. Johnston[1, 2]

[1]Melbourne Brain Centre Imaging Unit, The University of Melbourne, [2]Department of Biomedical Engineering, The University of Melbourne, [3]Melbourne Neuropsychiatry Centre, The University of Melbourne, [4]Department of Radiology, Royal Melbourne Hospital

Introduction

Spatially selective RF excitation pulses have been used previously to encode MR images using non-Fourier basis sets such as wavelet encoding and SVD decomposition [1,2,3]. We exploit the linear response model[4] of selective excitation and introduce double-RF pulses that encode the magnetisation using sinusoidally-modulated waveforms. We present a proof-of-principle that together, these excitation profiles generate the traditional Fourier encoding basis and a 3DBEE image volume can be directly recovered by inverse Fourier transform.

Theory and Methods

In 3D image acquisition, the signal at every point in kspace can be formulated as:

$$S(k_x, k_y, k_z) = \int_x \int_y \int_z M(x,y,z) e^{-jk_x x} e^{-jk_y y} e^{-jk_z z} \ , \qquad (1)$$

where $M(x,y,z)$ is the underlying magnetization and k_x,k_y,k_z are kspace coordinates. Substituting $e^{-jk_z z} = cos(k_z z) - jsin(k_z z)$ in Eq. 1 yields:

$$S(k_x, k_y, k_z) = \int_x \int_y \int_z M(x,y,z) e^{-jk_x x} e^{-jk_y y} \left(\cos(k_z z) - jsin(k_z z)\right) \ , \qquad (2)$$

The cosine and sine terms in Eq. 2 can be moved to the RF excitation profile, eliminating the need to use gradient encoding in the slice direction. Cosine and sine modulated slice profiles can be achieved by double-RF pulses with variable time shifts, Δ. Fig. 1 shows exemplar double-pulses with their corresponding cosine-modulated slice profiles. Sine-modulated profiles are achieved by applying phases of 90° and -90° to the first, and second pulse respectively.

An in-house 3D printed resolution phantom was scanned using 3DBEE via a modified Flash sequence (slab thickness = 7 mm, 21 slices of thickness = 0.33 mm, TE = 20 ms, TR = 500 ms, BW= 390 Hz/pix, FA = 15°, in-plane resolution = 0.78 × 0.78 mm, scan time = 47 minutes). For comparison the phantom was also scanned using a 3D FLASH sequence with the same parameters.

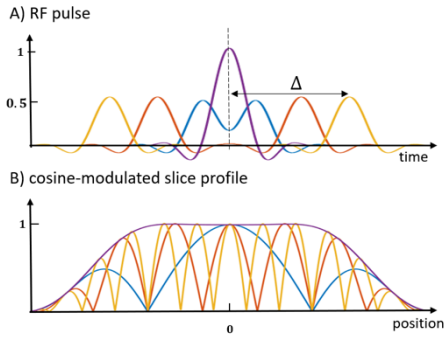

Figure 1: A) Exemplar double-RF pulses with variable time shifts, Δ. B) cosine-modulated slice profiles.

Results

Fig. 2 shows exemplar axial (A) and sagittal (B) slices of the phantom acquired using 3DBEE and 3D FLASH. Both the same contrast and structural information is achieved.

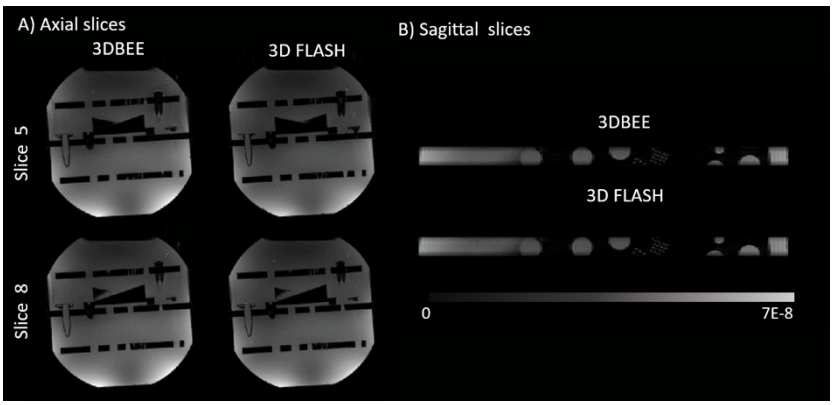

Figure 2: Exemplar A) Axial and B) Sagittal slices of 3DBEE and FLASH

Discussion and Conclusion

The 3D Basis Encoded Excitation (3DBEE) acquisition method has been demonstrated using double-RF pulses. The double-

RF pulses generate sinusoidally-modulated excitation profiles with variable frequencies that fill the traditional slice-phase-encode dimension of 3D kspace. The pulses used in the acquisition have half the SAR of the slab selective pulsed applied in conventional 3D acquisition. Ongoing work is demonstrating the advantage of 3DBEE over 3D conventional encoding for slice accelerated parallel imaging.

References

[1] Bolinger and Leigh. JMR. 1988. [2] Gelman and Wood.MRM.1996. [3] Panych et a. lMRM.1996. [4] Panych et al. Int J Imaging Syst Technol.1999.

Interactive AI-assisted labelling for abdominal MRI organ segmentation – **Xincheng Ye**

***Xincheng Ye*[1], *Fernanda L Ribeiro*[1], *Xiangyun Zhu*[1], *Trevor A Mori*[2], *Lawrence J Beilin*[2], *Steffen Bollmann*[1]**

[1]School of Information Technology and Electrical Engineering, The University of Queensland; Australia

[2]Medical School, The University of Western Australia; Perth; Australia

Introduction

Abdominal organ segmentation is a common task for analysing MRI data for various applications. However, annotating 3D organ volumes is time-consuming and needs anatomical expertise. Deep learning offers an opportunity to automate this task but requires large amounts of training data. To save time in generating training datasets, new AI-assisted labelling methods have evolved, such as MONAI Label [1]. There are two interactive models available through MONAI Label: *deepedit* and *deepgrow*. However, these models are both trained on CT data, and are not readily applicable for MRI data. In this work, we adjust *deepedit* and *deepgrow* for an abdominal MRI dataset to investigate the effectiveness of interactively annotating organs to build a large training dataset for automated segmentation.

Methods

The dataset includes T2-weighted abdominal Dixon MRI images from 975 Gen2 participants at 27-years of age from the Raine Study in Perth, WA, using a Siemens Magnetom Espree 1.5T (Siemens AG, Erlangen, Germany). The Dixon sequence yields both water and fat intensity data; for organ labelling, we use the water images. As a pre-processing step, we applied intensity normalization to all images. We modified and interactively trained *deepedit* and *deepgrow* on a small subset of the dataset – 16 images for training, 4 images for validation, and 9 images for testing. We manually labelled the pancreas. Then, we trained *deepedit*, *deepgrow 2d*, and *deepgrow 3d* interactively using an NVIDIA T4 GPU accelerator and Neurodesk [2]. Finally, we determined model's performance of three algorithms: *deepedit*, *deepgrow 3d*, and *deepgrow pipeline* (combination of *deepgrow 2d* and *deepgrow 3d*). For *deepedit*, we used a fully automated inference, while for *deepgrow* we used semi-automated inference through guide points.

Results

First, we found that the default intensity transform (originally designed for CT data) is not suitable for MRI data and we had to remove it from the pipeline of all models. Next, we evaluated the models' performance in terms of training time, inference time, and Dice coefficients. Table 1 lists the training time and inference time. Figure 1 shows the Dice coefficient of the testset; a prediction of *deepedit* is shown in Figure 2 as an example.

Table 1Training and inference time for all used models

	deepedit	deepgrow2d	deepgrow3d	deepgrow pipeline
train	44 mins	11 mins	7 hrs 56 mins	
infer	0.9 s/3D	0.7 s/2D	2.1 s/3D	5 s/3D

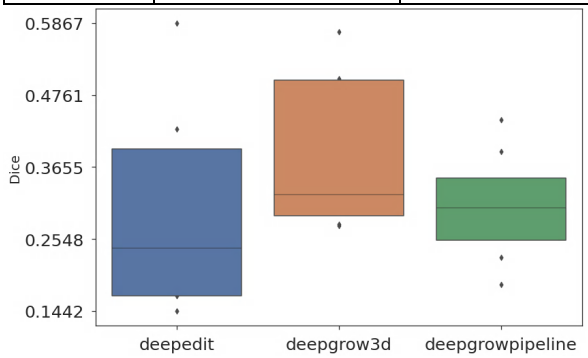

Figure 1 Dice coefficient of testset

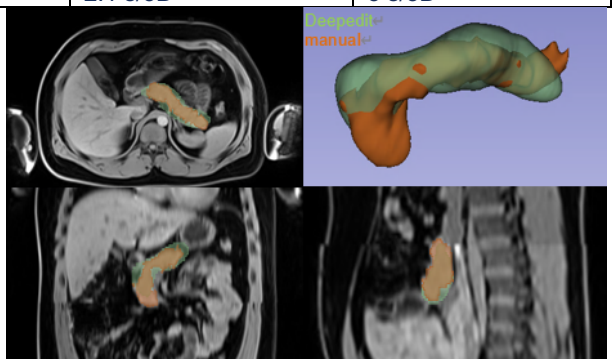

Figure 2 Prediction vs Manual Label

Discussion and Conclusion

D*eepgrow 3d* generated, on average, the best prediction for the pancreas but with the longest training time and *deepedit* had the most unstable accuracy. *Deepgrow 2d* showed a wide range of label noise across the abdomen and it was very time-consuming to select guide points. Furthermore, the *deepgrow pipeline* is very sensitive to guide points, making the prediction highly depend on user input. In conclusion, after pre-processing the MRI data, MONAI Label enabled the AI assisted generation of label data for abdominal MRI scans.

References

[1] A.Diaz-Pinto et al. MONAI Label: A framework for AI-assisted Interactive Labelling of 3D Medical Images. 2022. [2] Neurodesk. https://www.neurodesk.org

Acknowledgements

This work was supported by the Australian Research Council (LP200301393). The MRI data were acquired by Envision Medical Imaging, Perth WA. The Raine Study was funded by the NH&MRC (Mori, APP 1102106).

Efficient Network for Diffusion-Weighted Image Interpolation and Accelerated Shell Sampling – **Eric Pierre**

***Eric Y. Pierre*[1,2], *Kieran O'Brien*[2], *Thorsten Feiweier*[3], *Josef Pfeuffer*[3], *Daniel Staeb*[2]**

1. The Florey Institute of Neuroscience and Mental Health, Heidelberg, Australia. 2. MR Research Collaborations, Siemens Healthcare Pty Ltd, Australia. 3. MR Applications Predevelopment, Siemens Healthcare GmbH, Erlangen, Germany

Introduction

Fibre-tracking and fixel-based analyses are valuable neurological tools[1,2] but require long Diffusion Weighted (DW) acquisitions, often over 10 minutes even with multiband acquisitions[3]. However, skipping some DW directions and synthesizing their images offline[4,5] could provide high acceleration. This interpolation of DW images in q-space[4] can be done linearly on a voxel basis[5], but deep-learning networks could offer more accuracy and higher acceleration rates (R) from non-parametric diffusion models and local-neighbourhood information exploitation.

Methods

We developed a shallow, densely connected network using TensorFlow[6] illustrated in **figure 1**. It synthesizes N_{out} target DW-volumes on a per voxel basis from N_{in} acquired DW volumes, giving $R= N_{in} / (N_{in}+ N_{out})$. Each layer uses "reLU" activation. Training and validation datasets were respectively gathered from 20 and 40 subjects of the HCP database[7], with 90 directions at b=1000 s/mm², b=3000 s/mm², and a single b=0 s/mm² volume, with N_{in} = 31 and N_{out}= 60 for R≈3. Input DW-directions were chosen to best match a 3D golden angle sampling scheme. Training using a "MSE" loss-function was completed over 100 epochs on the MASSIVE supercomputer[8]. A linear spherical-interpolation model was also trained from the same datasets for comparison.

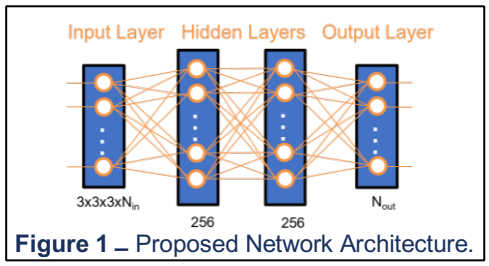

Figure 1 – Proposed Network Architecture.

Results

An example comparison of synthesized images is shown in **figure 2.** The target image as acquired by the scanner is referred to as gold standard. The linear model exhibits local errors in regions corresponding to important fibre tracks such as the optic radiations. In comparison, the network clearly reduces these errors.

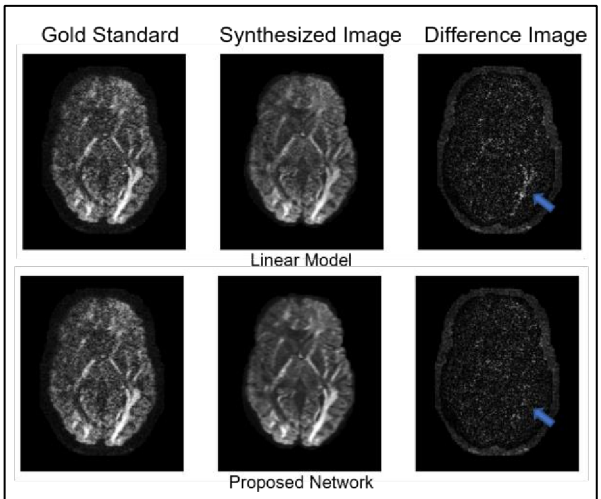

Figure 2 – Reconstruction at b=3000 s/mm²

Discussion&Conclusion

The proposed network is small but highly nonlinear and uses spatial-neighbourhood information. It appears to capture a better inherent diffusion model than linear interpolation approach. The small number of parameters allows fast, reproducible training without need for additional regularization. It is a promising approach for significantly accelerating data acquisition for connectome and fixel-based analysis, with results corresponding here to a threefold reduction in acquisition time.

References

1] Dhollander T et al. Neuroimage 2021;241:118417
2] Fornito A et al. . Nat Rev Neurosci. 2015;16:159–172
3] Tong Q et al. Sci Data. 2020; 7:157
4] Tuch DS. Magn Reson Med 2004; 52:1358–1372
5] Descoteaux M et al. Magn. Reson. Med. 2007;58:497–510
6] Abadi M et al. tensorflow.org
7] Rosen B et al. The Human Connectome Project (HCP) database. https://ida.loni.usc.edu/login.jsp 8] Goscinski WJ et al. Front Neuroinform. 2014;8

An Experimental Study of MRI Reconstruction using Transformer Networks - **Mevan Ekanayake**

***Mevan Ekanayake*[1,2], *Kamlesh Pawar*[1], *Mehrtash Harandi*[2], *Gary Egan*[1], *Zhaolin Chen*[1,2]**

[1]Monash Biomedical Imaging, Monash University, Melbourne, Australia

[2]Department of Electrical and Computer Systems Engineering, Monash University, Melbourne, Australia

Introduction

Long acquisition times are a significant limitation in the clinical utility of diagnostic MRI. Whilst acquisition times can be reduced by under-sampling the measurements in k-space, there is a resultant loss of quality in the reconstructed image. Recently, artificial intelligence and specifically deep learning models have been utilized to transform low-quality images into high-quality images by training the models on large cohorts of data. The self-attention-based transformer networks[1] have become the state-of-the-art in deep learning models. In this work, we assess the capability of transformer networks for accelerated MRI reconstruction and compare how the models perform in image and k-space domains.

Methods

Let y represent the fully sampled k-space and x represent its corresponding clean image. Then, x and y constitute a Fourier pair, i.e., $y = Fx$ and $x = F^{-1}y$ where F and F^{-1} represent the Fourier and inverse Fourier transforms respectively. In accelerated imaging, MR measurements are often undersampled resulting in an incomplete k-space, y_u and its corresponding aliased image, x_u. In this work, we analyse the capabilities of transformer networks for accelerated reconstruction between different pairs of domains: (a) image to image, (b) k-space to k-space, (c) k-space to image, and (d) image to k-space. Let T_θ be the mapping function representing the transformer network with parameters θ. Then the training processes for the above four models reduce to Eq. (1), (2), (3), and (4) respectively:

$$\theta_a^* = argmin_\theta\{L(x, T_\theta(x_u))\} \quad (1) \qquad \theta_b^* = argmin_\theta\{L(x, F^{-1}T_\theta(y_u))\} \quad (2)$$

$$\theta_c^* = argmin_\theta\{L(x, T_\theta(y_u))\} \quad (3) \qquad \theta_d^* = argmin_\theta\{L(x, F^{-1}T_\theta(x_u))\} \quad (4)$$

We implemented a cascade of Swin-Unets[2] with interleaved data consistency blocks as the mapping function, T_θ. We performed random 1D undersampling on k-space in the phase direction with an acceleration factor of 4. We utilized the l_1-norm as the loss function to train our models on 3096 T1W transverse brain slices (sampled from the fastMRI[3] dataset which were obtained on 3 and 1.5 Tesla MR scanners) for 100 epochs.

Results

Table 1 presents a quantitative evaluation of the validation set and Figure 1 depicts an example reconstruction.

Table 1: Average NMSE, PSNR, and SSIM scores evaluated on the validation set

Metric	***model (a)***	***model (b)***	***model (c)***	***model (d)***
NMSE	0.0055	0.0153	0.0349	0.0286
PSNR	39.51	35.13	31.54	32.33
SSIM	0.9487	0.9031	0.8534	0.8579

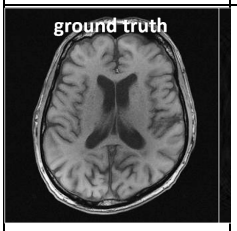

Fig 1: Reconstructions of a T1W transverse brain section from the validation set using (a) image to image, (b) k-space to k-space, (c) k-space to image, and (d) image to k-space transformer models.

Discussion & Conclusion

The quantitative and qualitative results confirm the capability of self-attention-based transformer networks to reconstruct high-quality images when utilized in an image-to-image mapping setting. Furthermore, k-space to k-space mapping performs better than the other cross-domain mappings. However, all models except image-to-image mapping lack the ability to accurately remove aliasing artefacts.

References

[1] Korkmaz et al. IEEE Transactions on Medical Imaging. 2020.
[2] Ekanayake et al. arXiv preprint. 2022.
[3] Zbontar et al. arXiv preprint. 2018.

Multi-parametric MRI to measure the oxygen partial pressure and the fluid viscosity of the vitreous humour of the eye - **Xingzheng Pan**

Xingzheng Pan[1]**,** *Renita Martis*[1]**,** *Beau Pontre*[2]*, Mohammed Ziaei*[3]*, Linley Nisbet*[4]*, Paul Donaldson*[1]*, Julie Lim*[1]

1. Department of Physiology, School of Medical Sciences, New Zealand Eye Centre, University of Auckland, New Zealand
2. Department of Anatomy and Medical Imaging, School of Medical Science, Faculty of Medical and Health Sciences, University of Auckland
3. Department of Ophthalmology, School of Medicine, Faculty of Medical and Health Sciences, University of Auckland
4. Auckland Bioengineering Institute, University of Auckland

Introduction

Vitreous humour is a clear gel-like fluid that fills the space between the lens and the retina to support the structure of the eye, which has been found to play an essential function in oxygen regulation and distribution within the eye recently. As the vitreous undergoes age-related liquefaction or is surgically removed (vitrectomy), this function is impaired, resulting in increased intraocular oxygen tension and the increased risk of age-related eye diseases. However, approaches to measuring oxygen levels in the vitreous humour involve invasive methods. In this study, we utilised MRI T1 and T2 mapping, along with experimental approaches to measure the oxygen partial pressure (pO_2) and the viscosity of the vitreous in a non-invasive manner.

Methods

Oxygen phantom (n = 3) was made of distilled water bubbled with nitrogen to vary the pO_2, ranging from 10 mmHg to 86 mmHg. pO_2 was measured with an oxygen-sensitive fibreoptic probe (Oxylite, Oxford optronic). The phantom was scanned by a 3T clinical MRI (VIDA, Siemens) equipped with a 32-head head channel. All imaging sequences had a Field of View (FOV) of 140 × 140 mm and a matrix size of 384 × 384. T1 mapping utilised a turbo-spin echo (TSE) with inversion recovery at six different inversion times (TI): 50, 860, 1880, 3240, 5340 and 10000 ms, and with a constant repetition time (TR) of 16000 ms and echo time (TE) of 8.6 ms. The T2 mapping utilised the same TSE with different TEs at 175, 400, 650, 900, 1150, 1400 and 1630 ms with a constant TR of 12000ms. Acquired images were fitted to calculate the T1 and T2 values using customised-written codes. T1 values were correlated with the measured pO_2 of the phantom[2], while T2 values were correlated with the viscosity measurements using our established methods[1]. NZ white rabbits (N=3) were used to pharmacologically induce vitreous liquefaction by intravitreal injection of hyaluronidase (0.25U/ml) in the right eye (treated). The left eye was untouched as it was the control eye (control). Rabbits were scanned after 8 weeks of the initial injection to measure pO_2 and the viscosity of the vitreous in control versus treated eyes.

Results

After adjusting the measured T1 with a temperature calibration[2], there was a strong positive relationship between R1 (1/s) and pO2 (mmHg). The calibration was characterised by $R1 = pO_2 \times 2.18e^{-3} + 0.199$ [R^2 = 95.6%]. The R2 (1/s) also highly correlated with the viscosity measurement: storage modulus (G'), loss modulus (G") and complex viscosity (η^*)[1]. The measured R1 and R2 of the rabbit eye were converted to pO_2 and viscosity. The treated eye revealed increased pO_2 levels compared to the control eye [Control: 16.27 ± 2.45 mmHg, Treated: 23.62 ± 3.95 mmHg] and decreased viscosity as evidenced by lower G' [Control: 0.23

± 0.03 Pa, Treat: 0.09 ± 0.01 Pa] , G" [Control: 0.16 ± 0.02 Pa, Treat: 0.09 ± 0.01 Pa] and η^* [Control: 0.03 ± 0.004 Pa, Treat: 0.013 ± 0.001 Pa] values compared with the control eye.

Discussion

Hyaluronidase breaks down the collagen network that progressively liquefies the vitreous body to increase vitreous pO2 levels and decrease viscosity. Our MRI protocols could accurately detect these changes in our rabbit model of vitreous liquefaction.

Conclusion

We have developed a non-invasive MRI-based technique that has the potential to be implemented clinically to investigate changes to the vitreous *in-vivo*. Our next step is to utilise our technique in human participants to monitor changes to the vitreous caused by normal ageing and/or vitreous removal to identify strategies that minimise pO2 levels and preserve overall ocular health.

References

1. Thakur et al. Exp Eye Res. 2020
2. Muir et al. Radio. 2012

Computationally efficient multi-echo QSM - **Korbinian Eckstein**

***Korbinian Eckstein*[7], *Thanh Thuy Dao*[7], *Ashley Stewart*[1,7], *Simon Robinson*[2,3,4,5], *Josef Pfeuffer*[6], *Kieran O'Brien*[6], *Jin Jin*[6], *Markus Barth*[1,2,7], *Steffen Bollmann*[1,2,7]**

[1]ARC Training Centre for Innovation in Biomedical Imaging Technology, University of Queensland, Brisbane, Queensland, Australia [2]Centre for Advanced Imaging, University of Queensland, Brisbane, Australia [3]Department of Neurology, Medical University of Graz, Graz, Austria [4]Karl Landsteiner Institute for Clinical Molecular MR in Musculoskeletal Imaging, Vienna, Austria [5]Department of Biomedical Imaging and Image-Guided Therapy, High Field MR Center, Medical University of Vienna, Vienna, Austria [6]Siemens Healthineers, Australia [7]School of Information Technology and Electrical Engineering, The University of Queensland, Brisbane, Queensland, Australia

Introduction

Numerous algorithms were developed to solve the dipole inversion problem of QSM, however, they generally share a long computation time. With multi-echo acquisitions becoming more popular for QSM, one way of combining the information into one volume is to average the final QSMs [1-2], which multiplies the computation time by the number of echoes. A range of Laplacian based methods for combining echo data before dipole inversion were investigated previously [3], but using a quantitative unwrapping procedure could have significant benefits over Laplacian methods. Here, we investigate how a quantitatively unwrapped multi-echo phase combination performs for combining multi-echo data for QSM processing.

Methods

Two datasets were used, the in-silico head phantom in 1mm isotropic resolution from the QSM challenge [4] and an in-vivo data set acquired at 7 T, where coil-combination and phase offset removal were performed using ASPIRE [5]. We compare four different QSM processing pipelines, i) *Laplacian - Weighted-average QSM*, where the multi-echo QSM data was averaged in the end, ii) *ROMEO - Weighted-average QSM*, where the unwrapping was performed using ROMEO [6], iii) *Laplacian - Combined Phase*, where the echo-combination was performed directly on the unwrapped phase, and iv) *ROMEO B0 - Combined*, where ROMEO B0 estimation was applied. Inverse-variance-weighted echo-combination was applied to combine phase and QSM respectively, and the same mask was applied in all pipelines. The mask was obtained by thresholding the phase quality map from the quantitative unwrapping procedure ROMEO. The background field correction vsharp and the Dipole inversion RTS [7] were performed on all pipelines using QSM.jl [https://github.com/kamesy/QSM.jl].

Results

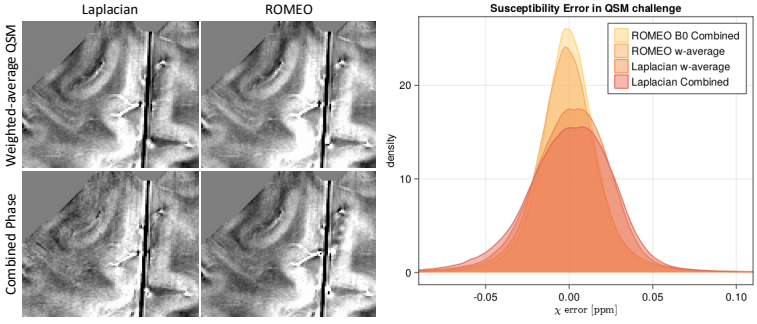

Left Figure: Laplacian Combined Phase has reduced SNR compared with the other approaches. This is less visible in areas of high phase SNR (not shown).
Right Figure: The distribution of the susceptibility error as a difference to the ground truth of the simulated QSM challenge dataset.

The ROMEO approaches were more accurate on the QSM challenge data. With in-vivo data, the visual appearance was similar with all 4 pipelines in regions of high phase SNR, while Laplacian – Combined Phase was affected by higher noise in regions of lower phase SNR.

Discussion and Conclusion

Background field removal and dipole inversion are usually the most time-consuming steps, and both are reduced by a factor corresponding to the number of echoes in the Combined Phase approaches. However, directly combining the phase after Laplacian unwrapping leads to reduced SNR in the QSM. This doesn't affect the ROMEO B0 approach, enabling efficient and high SNR QSM calculation. The ROMEO B0 calculation requires phase offset removal, which was performed by the computationally efficient ASPIRE method. The greatly reduced runtime might benefit transition into clinical practice.

References

[1] Caan et al. Hum Brain Mapp. 2019. doi: 10.1002/hbm.24490
[2] Stewart et al. Magn Reason Med. 2021. doi: 10.1002/mrm.29048
[3] Biondetti et al. Magn Reason Med. 2021. doi: 10.1002/mrm.29365
[4] QSM Challenge 2.0 Organization Committee et al. Magn Reason Med. 2021. doi: 10.1002/mrm.28754
[5] Eckstein et al. Magn Reason Med. 2018. doi: 10.1002/mrm.26963
[6] Dymerska et al. Magn Reason Med. 2021. doi: 10.1002/mrm.28563
[7] Kames et al. NeuroImage. 2018. doi: 10.1016/j.neuroimage.2017.11.018

Establishing baseline diffusion and susceptibility measurements for deep grey matter structures - **Manon Levayer**

Manon M.S. Levayer[1], Tonima S. Ali[1,2]

1. School of Biomedical Engineering, The University of Sydney, Australia; 2. Brain and Mind Centre, The University of Sydney, Australia

Introduction

Structures of the deep grey matter (DGM) play crucial roles in cognitive, sensory, and motor functions. MRI has vastly improved our knowledge on brain anatomy and functionalities in recent years, however, less is known about the DGM than other parts of the brain, such as the cortex. Neurodegenerative disorders such as Alzheimer's and Parkinson's diseases are known to implicate DGM structures such as the globus pallidus, putamen, thalamic nuclei and caudate[1,2]. MRI is sensitive to the changes caused by these pathologies (e.g., demyelination, iron deposition, etc) and specialised techniques, like diffusion-weighted imaging (DWI) and quantitative susceptibility mapping (QSM) can probe the structural and compositional properties of DGM and allow MRI-based characterisation[1-4]. This project evaluates DGM structures using multi-contrast MRI to assess microenvironments specific to individual DGM structures, with a goal of establishing baseline values for DGM in normal brains.

Methods

Images were acquired for 5 healthy subjects, with a 3T MRI scanner (Prisma, Siemens Healthcare, Erlangen, Germany) and a 64-channel head coil using NODDI protocol[2]. Diffusion-weighted images (DWI) were taken with b-value 0 (8 averages)/1000 (27 directions)/2500 (62 directions) smm^{-2}, 2 mm^3 isotropic resolution, 75 ms TE and 4.1 s TR. 3D Gradient echo (GRE) data was obtained in the same session, using 18° flip angle, 124 ms TR and 1.25 mm^3 isotropic resolution, Magnetisation Transfer (MT) ON (15 echoes with 2.37 – 52.63 ms TE) and MT OFF (25 echoes with 2.37 – 120 ms TE). DWI were processed using MRTrix 3.0[3], QSM with QSMxT[4] and Magnetisation Transfer Ratio (MTR) with Matlab (R2022a, Mathworks, Natick, MA). For each subject, DGM structures were isolated using Freesurfer segmentation (using T1w images from the same subjects) and mean values were measured for fractional anisotropy (FA), mean diffusivity (MD), QSM, and MTR.

Results (C = Caudate, PU = Putamen, PA = Pallidum, T = Thalamus)

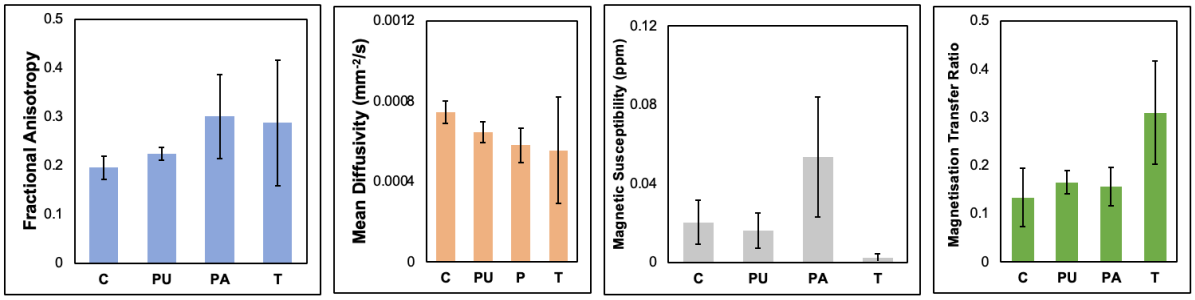

The figures above show FA, MD, Magnetic Susceptibility (MS) and MTR for the caudate, putamen, pallidum, and thalamus. The Pallidum was found to have the highest FA and MS, while the thalamus displayed low MD and MS but the highest MTR. The error bars suggest that the parameters measured from thalamus had higher variability across subjects for all but the MS.

Discussion and Conclusions

The thalamus also contains less iron than the other structures, which is reflected in its lower magnetic susceptibility[5]. Furthermore, it is known that in white matter, diffusivity is negatively correlated with anisotropy[1], and this was found to also be true in deep grey matter for some structures. To note, parameters measured from each DGM structure were consistent across subjects. This work demonstrates the potentials for establishing baseline diffusion and susceptibility scores for DGM structures. Having these baseline values can facilitate the MRI-based evaluation of DGM structures in future, whether normal or pathological. In the future, we will incorporate data from a large cohort for the results to represent normal population.

References

1. Pfefferbaum et al. *J Neurobiol Aging.* 2010. **2.** Zhang et al. *Neuroimage.* 2012. **3.** Tournier et al*. Neuroimage.* 2019. **4.** Stewart et al. *Magn Reson Med.* 2022. **5.** Gong et al. *J Neurobiol Aging.* 2014

Altered network topology in patients with visual snow syndrome: a resting-state 7 Tesla MRI study - **Myrte Strik**

M. Strik[1], M. Clough[2], E.J. Solly[2], R. Glarin[1], O.B. White[2], J. Fielding, and S.C Kolbe[2]

[1]Melbourne Brain Centre Imaging Unit, Department of Radiology, Melbourne Medical School, University of Melbourne, Melbourne, Australia.
[2]Department of Neuroscience, Central Clinical School, Monash University, Melbourne, Australia.

Introduction

Visual snow syndrome (VSS) is a neurological disorder characterized by a range of continuous visual disturbances. Little is known about the functional pathological mechanisms underlying VSS and their effect on brain network topology. The aim of this study was to characterize network dynamics in VSS patients using high-resolution resting-state (RS) 7T MRI.

Methods

Forty VSS patients and 60 controls underwent RS MRI. Functional connectivity matrices were calculated, and global efficiency (network integration), modularity (network segregation), local efficiency (connectedness neighbours) and eigen vector centrality (significance node in a network) were derived using a dynamic approach (temporal fluctuations during acquisition) (Figure 1). Network measures were compared between groups, with regions of significant difference correlated with known aberrant ocular motor VSS metrics in VSS. Lastly, nodal co-modularity, a binary measure of node pairs belonging to the same module, was studied.

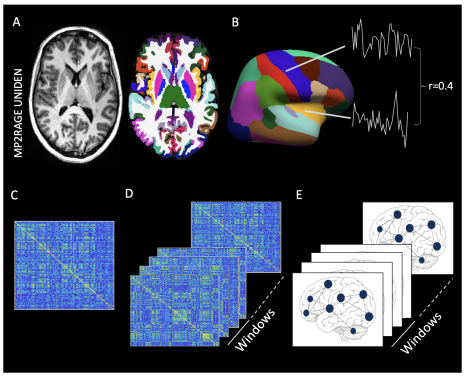

Figure 1. Overview network analyses pipeline.

Results

VSS patients had lower modularity, supramarginal centrality and local efficiency dynamics of multiple (sub)cortical regions, centred around the occipital and parietal lobules (Figure 2). Local efficiency dynamics of the lateral occipital cortex correlated with shortened prosaccade latencies in VSS patients (p=0.041, r=0.353). Further, in VSS patients, occipital, parietal and motor nodes belonged more often to the same module and demonstrated lower nodal co-modularity with temporal and frontal regions (Figure 3).

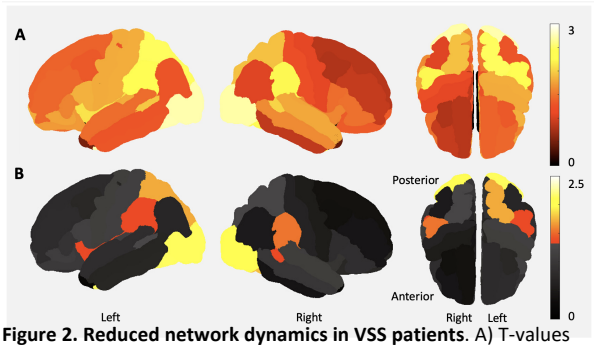

Figure 2. Reduced network dynamics in VSS patients. A) T-values and B) *p*-values (–log10) for group comparisons of local efficiency dynamics between controls and VSS patients.

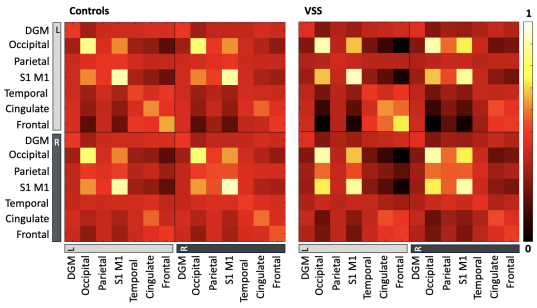

Figure 3. Conodal modularity. The colour indicates the proportion of subjects where node pairs were members of the same module. Abbreviations: DGM=deep grey matter, S1=primary somatosensory cortex, M1=primary motor cortex.

Conclusion

This study revealed reduced dynamic variation in modularity and local efficiency strength in VSS patients, suggesting that brain network dynamics are less variable in terms of segregation and local clustering. Changes were widespread, but strongest effects were observed in occipital cortices, related to oculomotor motor processing.

Functional and structural brain network development in children with attention deficit hyperactivity disorder - **Shania Soman**

Shania Mereen Soman[1], Nandita Vijayakumar[1], Phoebe Thomson[2,4], Gareth Ball[3], Christian Hyde[1], Timothy J. Silk[1,2]

[1]School of Psychology, Deakin University, Australia

[2]Child Mind Institute, New York, NY 10022, United States

[3]Murdoch Children's Research Institute, Melbourne, Australia

[4]Department of Paediatrics, University of Melbourne, Melbourne, Australia

Introduction

Attention deficit hyperactivity disorder (ADHD) is a prevalent childhood neurodevelopmental disorder. The application of graph theory to functional and structural connectomes has enhanced the understanding of functional and structural differences/alterations in neurodevelopmental disorders. Given the profound brain changes that occur during childhood and adolescence, it is important to examine longitudinal changes of both functional and structural brain connectivity across development in ADHD. This study aimed to examine the development of functional and structural connectivity in children with ADHD compared to controls using graph metrics.

Methods

175 individuals (91 children with ADHD and 84 non-ADHD controls) participated in a longitudinal neuroimaging study with up to three waves. The whole brain functional and structural connectivity matrix for each subject was defined using the multi-modal parcellation of human cerebral cortex (HCP-MMP) atlas.Graph metrics such as degree, local efficiency and betweenness centrality were extracted using Brain connectivity toolbox[2] from 370 resting state fMRI (197 Control, 173 ADHD) and 297 diffusion weighted imaging data (152 Control, 145 ADHD) acquired between the ages of 9 and 14. The developmental changes of each graph theoretical measure in children with ADHD vs typically developing controls were examined with Generalized Additive Mixed Models (GAMM), using the "mgcv" package in R.

Results

Compared to typically developing children, children with ADHD showed significant group differences and differential developmental trajectories for degree, local efficiency (LE) and betweenness centrality (BC), predominantly in higher-order cognitive and sensory regions such as anterior cingulate, posterior cingulate, frontal opercular cortex, superior temporal gyrus, inferior parietal cortex and visual regions.

Discussion

Our study demonstrated topology of functional and structural connectomes that mature differently between typically developing controls and children with ADHD across childhood and adolescence. In particular, similar networks of the brain, predominantly featuring higher-order cognitive and sensory regions, were affected in the functional and structural topology of children with ADHD relative to typically developing children, providing

converging evidence that structural and functional connectivity in these cortical regions are strongly implicated in children with ADHD.

Conclusion

Our findings indicate that the differential development of functional and structural connectivity observed in the brain regions involved in transferring neural signals across and between multiple higher order cognitive and sensory regions may be one explanation for the various higher order cognitive dysfunctions in children with ADHD. However, future studies examining the association between structural abnormalities and neurocognitve measures in children with ADHD are required to explore this further.

References

1] Sporns. Dialogues Clin Neurosci. 2011.

Poster Presentations

Mapping the brain functional correlates of cue-reactivity in moderate-to-severe cannabis use disorder: A functional neuroimaging study – **Arush Arun**

Hannah Sehl*[1], Arush Arun*[1], Victoria Manning[2], Govinda Poudel[3] & Valentina Lorenzetti[1]

[1]Neuroscience of Addiction and Mental Health Program, Healthy Brain and Mind Research Centre, Faculty of Health, Australian Catholic University, Melbourne, Australia, [2]Research and Workforce Development at Turning Point, Monash University, Melbourne, Australia, [3]Behaviour Environment and Cognition, Mary MacKillop Institute for Health Research, Australian Catholic University, Melbourne, Australia,

Introduction*:* Cannabis use disorders (CUD) are highly prevalent. Exposure to cannabis cues can trigger craving and compulsive use in people with a CUD and undermine their attempts cut down or quit[1]. fMRI findings in cannabis users exposed to cannabis cues vs neutral cues show different brain function and connectivity in prefrontal, striatal and parietal activity, in association with greater self-report craving. This study aims to characterise brain function associated with cue-reactivity (cannabis vs neutral cues) for the first time in cannabis users with a diagnosis of moderate-to-severe CUD vs controls, and how group differences in brain function are associated with cannabis craving and psychopathology symptoms.

Methods*:* All the pre-processing steps were performed using fMRIPrep 22.3[2]. To examine cannabis-specific cue reactivity differences between 49 people with a CUD (14 female) and 30 controls (15 female) aged 18-56 years; two subtraction contrasts were created: Can > Neutral and Can < Neutral and GLM was performed using SPM12. We explored how group differences in brain function correlated with: cannabis craving, CUD symptoms, arousal ratings of cannabis images and cannabis exposure metrics (i.e., dosage, duration of regular use, age of onset, abstinence duration).

Results*:* Greater activity was found in the CUD vs controls was found during exposure cannabis vs neutral images in the lingual gyrus (*FWE*-corrected), and in other areas - middle frontal gyrus, medial orbitofrontal cortex and cerebellum ($p < 0.001$; cluster $k > 10$). Positive correlations emerged between the activity of the middle frontal gyrus and cannabis grams/past month.

Discussion*: The brain pathways showed to differ in* CUD than controls, partly overlap with those reportedly altered in other substance use disorders and align to prominent

neuroscientific theories of addiction. Widespread brain activations during cannabis cue-reactivity may be ascribed to altered salience and attentional processes associated with CUD, and future longitudinal studies are required to elucidate if neurobiological alterations in CUD predate or follow CUD onset.

References: [1] Hindocha C, Freeman TP, Ferris JA, Lynskey MT, Winstock AR. No smoke without tobacco: a global overview of cannabis and tobacco routes of administration and their association with intention to quit. Front Psych. 2016;7:1-9. https://doi.org/10.3389/fpsyt.2016.00104 [2] Esteban O, Markiewicz CJ, Blair RW, et al. fMRIPrep: a robust preprocessing pipeline for functional MRI. Nat Methods. 2019;16(1): 111-116. https://doi.org/10.1038/s41592-018-0235-4

Investigating the computational reproducibility of Neurodesk - **Thanh Thuy Dao**

***Thanh Thuy Dao*[1], *Angela Renton*[1,3], *Aswin Narayanan*[2], *Markus Barth*[1], *Steffen Bollmann*[1]**

[1]School of Information Technology and Electrical Engineering, The University of Queensland, Brisbane, Australia; [2]Australian National Imaging Facility; [3]Queensland Brain Institute.

Introduction

Computational results of neuroimaging pipelines depend on the operating system being used due to version differences in underlying libraries, such as glibc. This reproducibility issue was quantified for several MRI analysis tools by Glatard et al[1]. Neurodesk (www.neurodesk.org) is a platform that aims to increase accessibility and reproducibility by packaging every pipeline into a software container and thereby can control the underlying dependencies regardless of the operating system. To evaluate the computational reproducibility of this approach, we compared brain tissue segmentation using FMRIB Software Library (FSL) on Neurodesk vs. Local installation on two different Linux distributions.

Methods

FSL 6.0.5.1 was built in Neurodesk and was natively run on two Linux systems resulting in 4 setups (Figure A). Local A: Ubuntu 20.04 with glibc 2.31, Local B: AlmaLinux 8.5 with glibc 2.2.8, and Neurodesk A and B: Ubuntu 16.04.7 with glibc 2.2.3. We segmented the cortical and subcortical structures of 157 T1-weighted magnetic resonance (MR) images from the International Consortium for Brain Mapping using FSL BET (brain extraction), FAST (tissue classification), FLIRT (image registration) and FIRST (subcortical tissue segmentation). The outputs from the four systems were compared pairwise: local system A vs B, Neurodesk on A vs B. System calls from FSL are recorded using ltrace for a single subject to validate that homogenizing the computing system resolves the reproducibility issue.

Results

The checksums showed that BET and FAST produced identical results inter-run and intersystem. For FLIRT and FIRST, the Dice coefficient indicated significant differences across local installations, while mostly remaining identical across Neurodesk setups (Figure B). The mismatch in subcortical segmentation occurred at the edges of each structure (Figure D). The records of library calls are different between locally installed FSL (Figure C) and were consistent across Neurodesk setups.

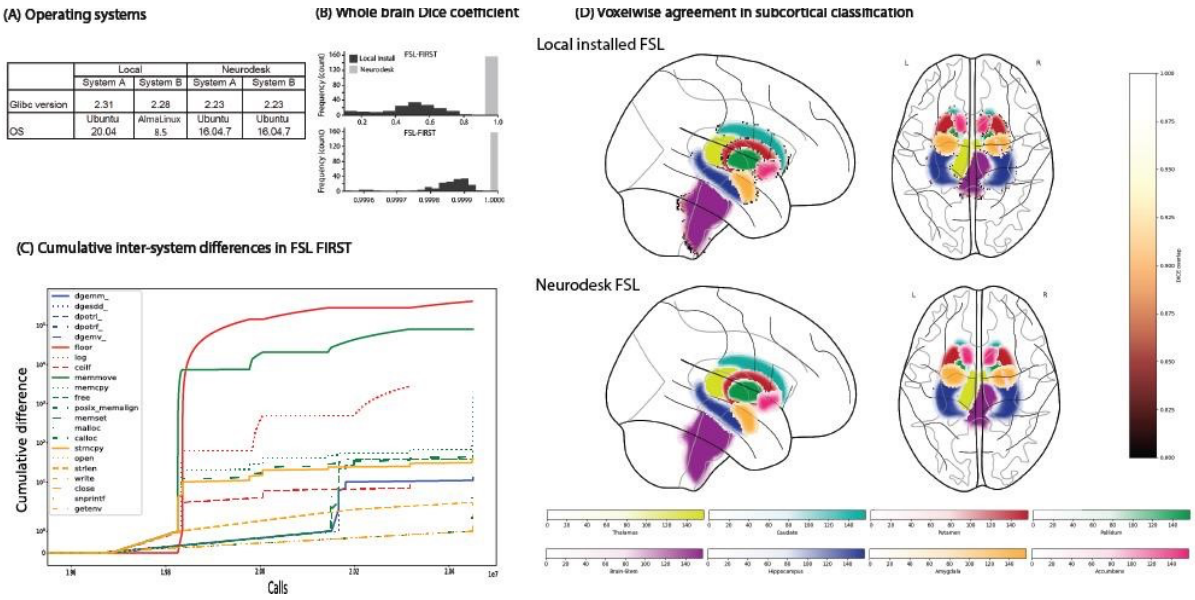

	Local		Neurodesk	
	System A	System B	System A	System B
Glibc version	2.31	2.28	2.23	2.23
OS	Ubuntu 20.04	AlmaLinux 8.5	Ubuntu 16.04.7	Ubuntu 16.04.7

Discussion and Conclusion

FSL is dynamically linked to use system libraries such as glibc and thus results may vary due to the system library version. The library call records indicate that the system version has a significant effect on reproducibility. Neurodesk addresses the reproducibility issue for dynamically linked tools by maintaining the same system version across computing environments.

References

[1] Glatard T, Lewis LB, Ferreira da Silva R, et al. Reproducibility of neuroimaging analyses across operating systems. *Frontiers in Neuroinformatics*. 2015

Adiabatic pulse approximation using a Fourier approach - **Edward Green**

***Edward M Green*[1], *Bahman Tahayori*[2], *James C Korte*[3,4], *Yasmin Blunck*[1,4], *Leigh A Johnston*[1,4]**

1. Melbourne Brain Centre Imaging Unit, The University of Melbourne, Melbourne, Australia, 2. The Florey Institute of Neuroscience and Mental Health, Melbourne, Australia, 3. Department of Physical Sciences, Peter MacCallum Cancer Centre, Melbourne, Australia, 4. Department of Biomedical Engineering, University of Melbourne, Melbourne, Australia

Introduction

Adiabatic pulses are commonly used in ultra-high field imaging for their insensitivity to B_1 field inhomogeneity. For conventional RF pulses, the slice profile may be approximated by the Fourier transform of the pulse envelope for flip angles up to approximately 90°[1], however, this approximation is unable to describe adiabatic pulse behaviour. In this work we present a new method for approximating the slice profile produced by adiabatic pulses in the presence of a constant gradient.

Theory

Analysis of adiabatic pulses can be simplified if it is assumed that the angle between the bulk magnetisation and the *z*-axis is equal to that of the effective field produced by an adiabatic pulse. Under this assumption, the transverse magnetisation as a function of constant off-resonance frequency can be approximated by the Fourier transform of a function of the pulse envelope:

$$M_{xy}(\Delta\omega_0) \approx \int_0^t \omega_1(\tau)\cos(\alpha^{Ad}(\tau,\Delta\omega_0))e^{j\Delta\omega_0\tau}d\tau,$$

where M_{xy} is transverse magnetisation, $\Delta\omega_0$ is off-resonance frequency, ω_1 is the RF pulse envelope as a complex number, α^{Ad} is the angle of adiabatic pulse effective field with the *z*-axis and t is time.

Methods

The behaviour of the adiabatic approximation was investigated through comparison with Bloch equation simulations. The adiabatic approximation and Bloch equations were simulated using *ode45* in MATLAB (Natick, Massachusetts, USA). A sin/cos adiabatic half passage pulse[2] was investigated, with pulse duration = 4ms, maximum pulse frequency offset = 2.5kHz, and maximum pulse amplitude $\omega_1/2\pi$ = 2kHz. Pulses were simulated over off-resonance frequencies, $\Delta\omega_0/2\pi$ = [-5kHz, 5kHz] and pulse amplitude scaling factor, ξ = [0,2]. Pulse behaviour not in the adiabatic pulse regime was excluded from analysis. The adiabatic condition was defined as not being sufficiently satisfied when Q<5, where Q is the maximum value given by the ratio of the amplitude of the pulse's effective field, ω^{eff}, and the angular rate of the effective field,

$d\alpha^{Ad}/_{dt}$: Q = $\left|\frac{\omega^{eff}}{d\alpha^{Ad}/_{dt}}\right|$.

Results

The adiabatic approximation matched the Bloch simulation closely where Q > 5 (Figure 1a,c). In the region where Q > 5, the mean absolute difference between the approximation and the Bloch solution was 0.023, with a maximum difference of 0.26.

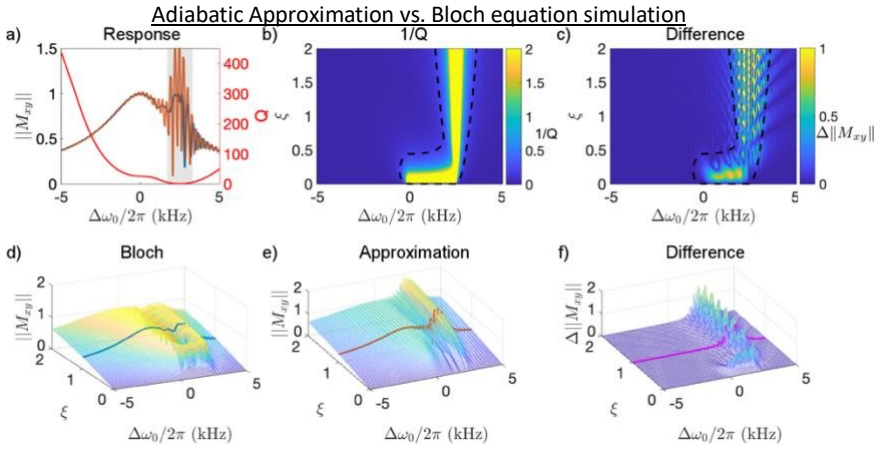

Figure 1: Transverse magnetisation for Adiabatic approximation (AA) vs. Bloch equation. AA (orange), Bloch (blue), adiabaticity factor Q (red). Q<5 indicated by grey in (a), and dashed region in (b,c).

Discussion

The proposed adiabatic approximation accurately calculates adiabatic pulse behaviour when the adiabatic condition is satisfied. Unsurprisingly, when Q < 5, magnetisation behaviour is less intuitive and may not be well-described by the adiabatic approximation. As the adiabatic approximation is represented by a form of the Fourier transform, the Fast Fourier Transform algorithm may be used to implement a rapid calculation framework for adiabatic pulse envelopes.

Conclusion

Our adiabatic approximation demonstrates the existence of a Fourier relationship between adiabatic pulse shapes and the resultant slice profile produced when adiabatic pulses are applied under constant gradient. This provides novel insight into adiabatic pulse behaviour and may be exploited for rapid calculation of adiabatic pulse envelopes.

References

[1] Pauly et al., J. Magn. Res., 1989. [2] Bendall & Pegg, J. Magn. Res., 1986.

Using quantitative susceptibility mapping (QSM) for clinical correlations of iron-rich deep grey matter of relapsing-remitting multiple sclerosis patients - **Ibrahim Khormi**

Ibrahim Khormi[1,2,3], Oun Al-iedani[1,2], Bryan Paton[1,2], Amir Fazlollahi[4,5], Jeannette Lechner-Scott[1,2,6], Abdulaziz Alshehri[1,2,7], Kieran O'Brien[8,9], Steffen Bollmann[9,10], Rishma Vidyasagar[11], Scott Ayton[11], Anne-Louise Ponsonby[11,12], Saadallah Ramadan[1,2]

[1]University of Newcastle, Newcastle, Australia, [2]Hunter Medical Research Institute, Newcastle, Australia, [3]College of Applied Medical Sciences, University of Jeddah, Jeddah, Saudi Arabia, [4]Queensland Brain Institute, The University of Queensland, Brisbane, Australia, [5] Department of Radiology, University of Melbourne, VIC, Australia, [6]John Hunter Hospital, New Lambton Heights, Australia, [7]Department of Radiology, King Fahad University Hospital, Imam Abdulrahman Bin Faisal University, Dammam, Saudi Arabia. [8]Siemens Healthcare Pty Ltd, Brisbane, Queensland, Australia,[9]ARC Training Centre for Innovation in Biomedical Imaging Technology, The University of Queensland, Brisbane, Queensland, Australia, [10]School of Information Technology and Electrical Engineering, The University of Queensland, Brisbane, Queensland, Australia, [11]The Florey Institute of Neuroscience & Mental Health, Parkville, VIC, Australia [12]Murdoch Children's Research Institute, Royal Children's Hospital, University of Melbourne, VIC, Australia

Introduction: MS demyelination and atrophy alter the tissue's diamagnetic properties leading to higher tissue magnetic susceptibility[1]. High levels of iron accumulation have been detected in the deep grey matter (DGM) structures of people with MS (pwMS)[1]. Quantitative susceptibility mapping (QSM) is a novel post-processing imaging modality that quantifies tissue magnetic susceptibility using a gradient-recalled-echo (GRE) sequence. We aimed to characterise the magnetic susceptibility in selected DGM structures with reference to medial-frontal white matter for pwMS and healthy controls (HCs). Correlation between DGM QSM metrics and selected MS clinical parameters was computed.

Methods: Five relapsing-remitting multiple sclerosis (RRMS) participants and nine age-matched HC were recruited (mean age: 46±14 yrs). MRI scans were performed on a 3T scanner. The STI Suite (v2.2) was used for QSM map reconstruction from 3D GRE images. The significant QSM differences associated with selected DGM structures were assessed using repeated-measures ANOVA controlling for the reference region. RRMS clinical measures included disease duration, cognitive, fatigue, mental health assessment, and Expanded Disability Status Scale. Correlations between clinical measurement scores and iron-rich regions, accounting for age, were performed using Pearson's correlation.

Results: The RRMS participants showed significantly higher susceptibility compared to HCs in the caudate (β= +26.2, p = 0.004), pallidum (β= +38.9, p = 0.006) with a trend toward significant for putamen (β= +21.2, p = 0.09), and significantly lower susceptibility in thalamus (β= –10.2, p = 0.04). For the RRMS cohort, pallidum, and thalamus QSM values were highly correlated with the anxiety scale (r=0.98, r=-0.93, respectively). The dentate nucleus and putamen were highly correlated with the disease duration (r=-0.93, r=-0.91, respectively) with $p<0.05$.

Discussion: These preliminary results present novel work assessing magnetic susceptibility variations across different DGM and their clinical correlations in RRMS. QSM signals in the pallidum and thalamus seem to be strongly correlated with anxiety scores, which is a frequent symptom of MS[2]. Cognitive impairment in MS has repeatedly been correlated with volume reduction in the thalamus[1]. The lower susceptibility in the thalamus region, compared to other regions, may come from lower paramagnetic iron components and higher diamagnetic components, potentially a consequence of demyelination[3]. Also, there were strong correlations between increasing disease duration with the dentate nucleus and putamen.

These findings confirm previous studies demonstrating links between the severity of disease duration and QSM values in some DGM regions [4].

Conclusion: These preliminary QSM results from pwMS suggest that neurodegenerative and neuroinflammatory processes in DGM (caudate, pallidum, putamen, thalamus, dentate nucleus) might lead to clinical symptoms. While the studied cohorts were small, our research supports the promising nature of QSM to investigate the contribution of iron in the pathophysiology of MS.

References: 1] Zivadinov et al. Radiology. 2018. 2] Fujiwara et al. American J. of Neuroradiology, 2017. 3] Jameen et al. J. of the Neurological Sciences.2019. 4] Langkammer et al. Radiology 2013.

Acknowledgements: This research was kindly supported by Medical Research Future Fund. The authors acknowledge the patients and healthy controls who participated in this study.
The authors acknowledge the facilities and scientific and technical assistance of the National Imaging Facility, a National Collaborative Research Infrastructure Strategy (NCRIS) capability, at the Hunter Medical Research Institute Imaging Centre, University of Newcastle.

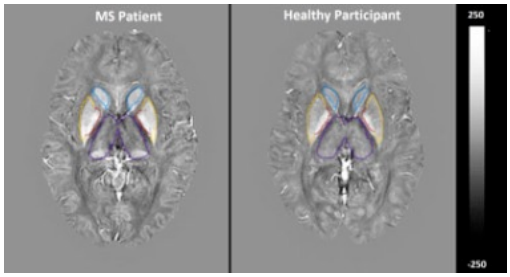

Figure 5 Figure 1. Quantitative susceptibility maps within thalamus (purple), caudate (blue), pallidum (red) and putamen (yellow) of a 38 years-old female RRMS vs. 40years-old female HCs.

Probabilistic Fixel-based White Matter Atlas - **Lea Vinokur**

Lea Vinokur[1,2], Robert E. Smith[1,2], Thijs Dhollander[3], Alan Connelly[1,2]

[1]The Florey Institute of Neuroscience and Mental Health, Melbourne, Australia, [2]Florey Department of Neuroscience and Mental Health, The University of Melbourne, Melbourne, Australia [3]Developmental Imaging, Murdoch Children's Research Institute, Melbourne, Victoria, Australia

Introduction: Fixel Based Analysis is being established as the state-of-the-art processing pipeline for [1] statistical analysis of white matter alterations, thus replacing lower-order models. However, it is evident that there is a need for a readily available anatomical reference atlas, such as those available for voxel-based models [2]. This often prompts researchers to perform manual dissection relying on expert input, or to perform complex and highly variable pipelines to translate available voxel-based information into the fixel space. To address this issue, we have constructed a probabilistic fixel-based atlas of 72 anatomically defined bundles represented on a fixel-based template, providing anatomical context, streamlining ROI selection, and assisting with the reproducibility of fixel-based statistics.

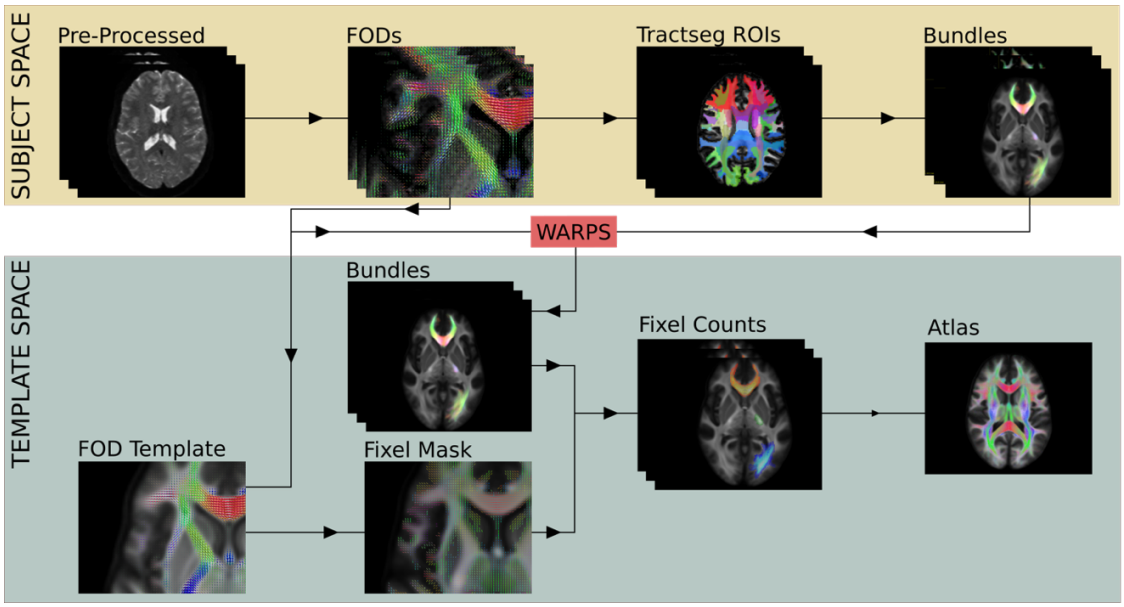

Fig.1: *A flowchart representing the different steps performed during atlas construction, as presented in the methods section.*

Methods: CSD was performed on the DWI data of 100 subjects from the HCP[3] pre-processed dataset to calculate FODs. The FOD images were then used to construct a population template[1] and calculate individual subject wraps from subject to template space. In addition, TractSeg [4] was performed on the FOD images all 100 subjects in subject space to extract voxel masks for the trajectories, start and end regions of 72 anatomical bundles. Trajectory masks were used for seeding, and start and end regions as inclusion regions for tractography, and the iFOD2 tracking algorithm was used to generate 20k streamlines per bundle. Individual subject warps from the template construction process were used to warp tractography results onto the fixel mask in template space and create individual binary fixel masks per-bundle, per-subject subject. The bundle masks were then aggregated across the 100 subjects to create weighted fixel masks for each of the 72 bundles represented on the fixel template.

Results: In this work, we delineate the steps taken to construct a fixel-based probabilistic atlas. The resulting atlas provides an anatomical reference for 72 major white matter tracts with weighted labelling at the fixel level.

Discussion: In addition to simple anatomical reference, the atlas can provide further utility to benefit the broader neuroscientific community. By enabling automatic anatomical parcellation, the atlas can assist with improving accessibility to and standardizing ROI-based fibre-specific analysis, enabling easy comparison across studies and with existing literature. The probabilistic aspect provides weighted bundle labels, while capturing inter-subject variability, encapsulating the complexity of white matter microstructure – thus potentially increasing both the specificity and sensitivity of such analysis.

1.Raffelt, D. A. *et al*., *Neuroimage* (2017). 2. Mori, S. *et al*., *Neuroimage* (2008). 3. Glasser, M. F. *et al. Neuroimage* (2013). 4.Wasserthal, J. *et al*, *Neuroimage* (2018).

A Feasibility Study of Semi-supervised Brain Tumour Segmentation using a Privacy Preserving Federated Deep Learning Framework - **Xinqian Wang**

Xinqian Wang[1], Yanjun Zhang[1], Steffen Bollmann[1]

[1]School of Information Technology and Electrical Engineering, The University of Queensland, Brisbane, Australia

Introduction

Federated Learning (FL) could enable the training of powerful algorithms across multiple institutions without sharing sensitive data. However, there are two main challenges for FL to be used for medical applications: first, even when distributing the annotation workload across multiple institutions it is still difficult to yield sufficient training data to train deep learning models; second, plain FL does not meet the privacy standards required for medical imaging data. With a plain FL training, each institution transfers their model parameters to a central server and the server averages the model parameters across institutions. Without additional security measures, such a mechanism leads to a model where potentially sensitive training data could be extracted from the model [1]. To tackle these two challenges, we combined a self-supervised learning task, AutoSeg [2], with a privacy-preserving FL algorithm, Confined Gradient Descent (CGD) [3].

Methods

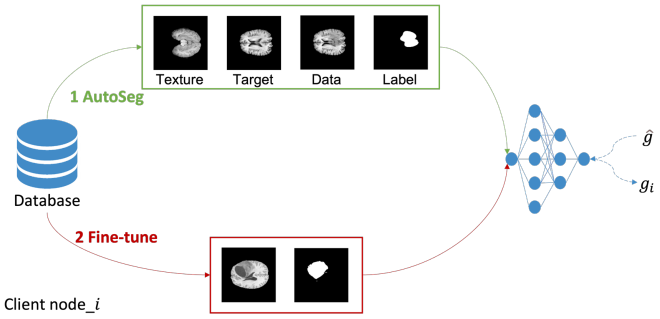

Fig.1 presents our method from the perspective of a single client node. The client node has many unannotated MRIs and few annotated MRIs. The client's goal is to utilise the unannotated MRIs to train a model and fine-tune the model based on the limited amount of labelled data. the whole training process is under the privacy preserving FL framework of CGD.

In the first step of Fig.1, the client randomly takes two unannotated MRIs to simulate data-label pairs using AutoSeg. For each iteration, the model randomly generates a batch of simulated lesion MRIs for training the model. Then the pretrained model is finetuned using real annotated MRIs.

Instead of plain federated learning (FedAvg), we utilized CGD, where each model first initializes their unique model parameters. Then, for each iteration (Fig.1 right), the client i computes its own gradient g_i based on its own data and own model. Next, it sends g_i to a central server. The central server aggregates the clients' gradients and sends $\hat{g} := \sum_{i=0}^{N} g_i$ back to each client model. Each client uses the same gradient $\hat{g}$ to update their unique model. Thus, at the end of the training, each client model trains a unique model. We tested a scenario where five clients jointly train their own brain segmentation model using a U-Net [4]. For each client, we allocate 337 slices of annotated MRIs and 1057 slices of unannotated MRIs from the BraTs'20 dataset and we kept the rest for testing (15172 MRI slices).

Results & Discussion

We found that the self-supervised learning with AutoSeg delivered a dice score of 0.45 and fine-tuning with real labels yielded a dice score of 0.7. Our results show that CGD (dice 0.68) performs comparable to FedAvg (dice 0.69) and both federated algorithms achieve a comparable dice score to the centralized training (dice 0.71). Our results indicate that such a framework could overcome the label shortage and protect confidential patient information.

Conclusion

Our study shows that it is possible to accelerate the training of a deep learning model in a privacy-preserving fashion using CGD in a task where five clients jointly train a semi-supervised brain tumour segmentation.

References

[1] Christopher G Schwarz, Walter K Kremers, Terry M Therneau, Richard R Sharp, Jeffrey L Gunter, Prashanthi Vemuri, Arvin Arani, Anthony J Spychalla, Kejal Kantarci, David S Knopman, et al. Identification of anonymous mri research participants with face-recognition software. New England Journal of Medicine, 381(17):1684–1686, 2019. [2] Felix Meissen, Georgios Kaissis, and Daniel Rueckert. Autoseg – steering the inductive biases for automatic pathology segmentation, 2022. [3] Yanjun Zhang, Guangdong Bai, Xue Li, Surya Nepal, and Ryan K L Ko. Confined gradient descent: Privacy-preserving optimization for federated learning, 2021.
[4] Olaf Ronneberger, Philipp Fischer, and Thomas Brox. U-net: Convolutional networks for biomedical image segmentation. CoRR, abs/1505.04597, 2015.

2D UTE imaging for rapid 23Na MRI - **Chengchuan Wu**

Chengchuan Wu, Yasmin Blunck, Leigh A. Johnston
Dept. Biomedical Engineering & Melbourne Brain Centre Imaging Unit, University of Melbourne

Introduction

Spin density-weighted sodium (^{23}Na) MR imaging for concentration quantification has been used in a range of clinical studies, such as stroke, multiple sclerosis and glioma[1]. However, the required scan time is long and hinders practical uptake of ^{23}Na MRI. Prolonged scan times can largely be attributed to the limitation of single receiver coils and 3D non-Cartesian sequences. Consequently, the images are prone to aliasing artifacts. Apodization can be used to suppress such artifacts, but it leads to broadened local partial volume effect (PVE)[2]. Compared to 3D acquisition, 2D imaging has a lower Nyquist limit and an explicit slice profile. For ^{23}Na MRI, the UTE-enabled half-pulse excitation (HPE)[3] can be used to capture the fast-decaying sodium signals. In this work, the use of HPE 2D projection reconstruction (PR) is compared with 3DPR in a short scan time (2.5 minutes) to assess efficiency and accuracy, and to enable recommendations for future rapid ^{23}Na-MRI experiments.

Methods

Phantom and in-vivo experiments were performed on a Siemens 7T Magnetom MRI scanner with a QED ^{1}H/^{23}Na head coil. A spherical **saline phantom** was scanned with a 2D imaging plane centred on a 6 mm PMMA disc containing a series of saline-filled holes. The **in-vivo brain** scan was performed on a healthy volunteer. **HPE 2DPR**: half pulse length = 3 ms, TE/TR = 0.25/150 ms for spin density weighting, readout = 16 ms, FOV = 200 mm, nominal in-plane resolution = 3.1 mm, thickness = 3.1 mm (5 mm for brain). Golden-angle readout spokes fully sampled the k-space in 2.5 mins. **Undersampled 3DPR**: 0.5-ms rectangular pulse, TE = 0.1 ms, nominal resolution = 3.1 mm-iso, all other parameters matched to 2DPR. In 2.5 minutes, 3D k-space was undersampled by a factor of 12. **Phantom preprocessing:** Spokes were density compensated and Tukey-filtered with parameter α = 0 (no apodization), 0.5 and 1 (Hann window). ***In-vivo* preprocessing:** A Turkey window (α = 0.5) was used. In addition, a densely sampled 3DPR image (25 minutes, α = 0) was used as the reference. Tissue concentration measurements were referenced to the CSF with an assumed value of 135 mM.

Results

Streaking artifacts were prominent only in the undersampled 3DPR images (Fig.1). Increasing the apodization reduced the streaking, as well as the background noise and Gibbs ringing, but it also smoothed the image structure. With α = 1, the streaking was considerably reduced in the phantom 3DPR. However, PVE from adjacent slices resulted in hyper-intensities in the signal-void region, whereas the 2DPR phantom images preserved contrast at α = 1, maintaining a suppressed background intensity.

The *in-vivo* 2DPR data showed better visual quality than the undersampled 3DPR image where the anatomical structure was degraded by the aliasing. The mean tissue sodium concentrations were 39.2±13.8 mM (2DPR) and 45.3±17.8 mM (3DPR), compared to the reference estimate of 37.2±8.8 mM.

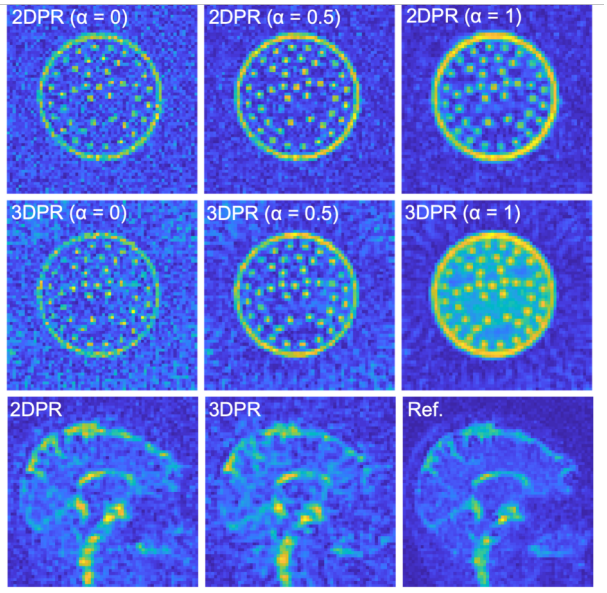

Figure 1: Reconstructed phantom & in-vivo

Discussion and Conclusion

Our comparison of 2DPR and 3DPR for fast ^{23}Na MRI demonstrated that undersampled 3DPR requires strong apodization to alleviate streaking artifact. This, however, inevitably exacerbates smoothing, at the detriment to quantitative capability of ^{23}Na MRI. With an apodization window, the measured tissue sodium concentration was elevated by ~22% compared to the reference. In contrast, the apodization was contained within the plane in 2DPR. The measured value in 2DPR increased by 5%, which included some extra contribution from the thicker 2D slice. For focused, fast sodium imaging, HPE 2DPR provides rapid acquisition and higher fidelity data.

References

[1] Madelin *et al*. Prog NMRS. 2014. [2] Pipe *et al*. MRM. 2000. [3] Pauly *et al*. JMR. 1989.